

3D NUMERICAL MODELS FOR ALONG-AXIS VARIATIONS IN DIKING AT
MID-OCEAN RIDGES

by

Xiaochuan Tian

A Thesis

Submitted in Partial Fulfillment of the
Requirements for the Degree of
Master of Science

Major: Geophysics

The University of Memphis

May, 2015

Copyright © 2015 Xiaochuan Tian

All rights reserved

Dedication

I would like to dedicate this thesis to my mother, Xia Tian. I wouldn't have a chance to experience this wonderful world without her giving birth to me. She rears me up by herself with her great love, optimism and peseverence. Without her guidance and support, I will not become who I am.

I also want to dedicate this thesis toward my major thesis advisor: Dr. Eunseo Choi. His mentorship defines what a great advisor is like. Without his guidance, neither this theis nor my fast personal-development during these two years is possible. He has kindled a flame that illuminates the way for my future career as a geodynamic modeler.

Acknowledgements

There is no proper words for me to express my deep gratitude toward my thesis advisor Dr. Eunseo Choi. He has changed my life in a very positive way. From him, I have learned what a great researcher and educator should be like. It is because of his unfailing care and understanding that have given me the courage to persevere, to carry on during the darkest days as an international student far away from home. It is his vivid and interesting lessons that have inspired me so much that I want to devote my career into geodynamic modeling. It is his numerous inspiration and encouragement that has motivated me to work super hard (enjoy at the same time) on the fascinating research questions. It is his altruistic share that has provided me with great chances to learn from great researchers, references, and to attend meetings. It is his patience to guide me through my endless silly questions that has nourished and cultivated my capabilities of being an independent researcher. Blessings from Eunseo, my role model, are countless. I will keep them in mind and try my best to relay the torch.

To the other two committee members, Dr. Christine Powell and Dr. Jer-ming Chiu, for their guidance and advice during many committee meetings. For their interesting courses.

To Center for Earthquake Research and Information and University of Memphis, thank a lot for providing me this great chance to study here with full tuition and graduate research assistanship. It is this kind support that has made my two year studies at this great institution possible. To all the faculties taught me courses and staff Josephine provided me a very pleasant, tidy and clean place for doing research and studying.

To students, Yangyang Naeem Sabber

To Center for Writing and Communication staff: Bill Schraufnagel To Tianhe2 super computer center, thank a lot for the support from National Supercomputer Center in Guangzhou. For about 200k Sus.

To Dr. Jie Liu and Dr. Ke Zhang, for kindly sharing their computing resources on Tianhe2.

To Dr. Gu Cheng,

To Shengfang Chen and Lijie Lyu

Finally, I want to thank my families, grandfather, grandgrandfather(ling zhong qian rang wo hao hao xue xi), grandma, mum.

“In the midst of winter, I found there was, within me, an invincible summer.”

—Albert Camus

“People have no higher calling than to strive for the greater good of humankind and society and that the future of humanity can be assured only when there is a balance between scientific development and the enrichment of the human spirit.”

—Kazuo Inamori

“不失其所者久，死而不亡者寿。”

—《道德经》

Abstract

Tian, Xiaochuan. M.S. The University of Memphis. May 2015 Master of Science.
3D Numerical Models for Along-axis Variations in Diking at Mid-Ocean Ridges. Major
Professor: Eunseo Choi.

Bathymetry of ocean floors reveals a great variety of morphologies at Mid-ocean Ridges (MORs). Previous studies showed that the morphologies at slow spreading MORs are mainly controlled by the ratio between rates of magma supply and plate extension. 2D models for the across-ridge cross-sections have been successful in explaining many of the observed morphological features such as abyssal hills and oceanic core complexes. However, the magma supply varies along the ridge and the interaction between the tectonic plates and magmatism at MORs are inevitably 3D processes. We propose to investigate the consequences of the along-axis variability in diking in terms of faulting pattern and the associated structures. This work will include implementation of an algorithm of parameterizing repeated diking in a 3D parallel geodynamic modeling code.

Table of Contents

Chapter	Page
1 Introduction	1
1.1 Review of Literature	1
1.2 Statement of Research Purpose	6
2 Methods	8
2.1 Method of approach	8
2.2 Model Setup	9
2.3 Parameters to control	10
3 Results	14
3.1 Reference model M28LinT1	14
3.1.1 Constant M along the ridge axis (M88ConT2 Table 2)	18
3.2 Main characteristics of the models	19
3.2.1 Location of termination	20
3.2.2 Geometry of the trough inside the median valley	21
3.2.3 Second fault	22
3.2.4 Fault alternation	22
3.2.5 Cut-back	22
3.2.6 Corrugations	22
3.3 Effects of the functional forms of M variation	23
3.4 Effects of the weakening rate	25
3.4.1 M58SinT1 versus M58SinT2	29
3.4.2 M58SqrtT1 versus M58SqrtT2	31
3.5 Effects of the range of M variation	33
3.5.1 M28SinT1 versus M57SinT1 versus M58SinT1	34

3.5.2	M57SinT2 versus M58SinT2	35
3.5.3	M28LinT1 versus M57LinT1	35
3.5.4	M28SqrtT1 versus M58SqrtT1	37
3.5.5	M57SqrtT2 versus M58SqrtT2	37
3.6	Summary of Results	38
4	Discussion	41
4.1	Discussion on Reference models	42
4.2	Cut Back	42
4.3	Fault Alternation	47
4.3.1	Trade-off between bending and weakening	47
4.3.2	Alternating on conjugate plate	48
4.3.3	Secondary near-axis normal fault	49
4.3.4	Effect of along ridge-axis coupling	49
4.4	Corrugations	50
4.4.1	Wavelength of corrugations	50
4.5	Influence of healing	50
4.6	Comparing model results with nature observation	50
4.6.1	Cut back at 13°N Mid-Atlantic Ridge (M28SqrtT1)	50
4.6.2	Double dome at 23°N Mid-Atlantic Ridge (Kane Megamullions) (Several models)	51
4.6.3	Atlantis Massif Shape at 30°N Mid-Atlantic Ridge ()	52
4.6.4	Shear low	52
4.6.5	Corrugations	52
4.7	Model Limitation	52
4.7.1	Fixed thermal structure effects and justification	52
4.8	Recommendation for Future Research	52

5 Conclusions **53**

Bibliography **54**

List of Tables

1	Summary of 3D Model Parameters	12
2	List of 3D numerical experiments.	13
3	Model behaviors in short.	39
4	Linear functional form.	39
5	Sinusoidal functional form.	39
6	Square root functional form.	40

List of Figures

1	Profiles of bathymetry across MORs.	2
2	Two bathymetry cross-sections of Mid-Atlantic Ridge (MAR) with 10 times vertical exaggeration. A-A' is closer to the ridge segment center while B-B' is at the tip of the segment near the Atlantis Transform fault.	3
3	Relationship between the maximum crustal thickness variations (ΔH_c) along a ridge segment and the segment length (L). The dashed line is the best-fit linear regression of the combined data. [Chen and Lin, 1999]	3
4	Upper one: modeling result for fast spreading agrees well with the observation of East Pacific Rise. Lower one: modeling result for slow spreading ridges agrees well with the bathymetry of Mid Atlantic Ridge. [Buck et al., 2005]	5
5	A~F: Faulting behaviors for different values of M. Geologic interpretation is superimposed on modeled distribution of strain rate. Dots show breakaways of initial faults. Dashed seafloor is original model seafloor, red dotted seafloor is formed dominantly by magmatic accretion, and solid bold is fault surface. Note that the detachment faults in B and C are not interrupted by secondary faults. [Tucholke et al., 2008]	6
6	Essential components of the numerical method.	9
7	Model setup	10
8	Evolution of plastic strain and surface topography of the reference model M28LinT1 (Table 2). Each snapshot shows plastic strain plotted on the model domain and the five times exaggerated topography. Initial seafloor is marked as a reference of 0 km of the topography. The bold dash lines (black) are the terminations of the detachment faults. The bold dash lines (red) in g) and h) are the transfer faults that connect the terminations along the ridge. The inset in f) plots plastic strain with opacity linearly proportional to its value.	14

9	Bird's-eye view of the evolution of breakaway (marked by green bold line) and depressed narrow zone along the ridge axis ("trough") (red dash line in (a)) for model M28LinT1 (Table 2). This figure share the same color scales with Figure 8.	15
10	Bending stress illustration. The blue line is the neutral plane where $\sigma_{xx} = 0$. Above the neutral plane is compression ($\sigma_{xx} < 0$) and beneath it is tension ($\sigma_{xx} > 0$). Due to sea water pressure and lithostatic pressure, compression is generally one degree magnitude larger than tension.	16
11	Bird's-eye view of velocity field with plastic strain plotted with opacity linearly proportional to its value. (color scale the same as Figure 8.a))	18
12	Bird's-eye view of σ_{xz}	18
13	Evolution of plastic strain and surface topography of the model: M88ConT2 (Table 2).	19
14	Five slices of strain rate along the ridge axis for the model M28LinT1 (Table 2) at 107.5 kyr. The 5 terminations and 5 breakaways along the ridge axis are marked by the 5 black and 5 red arrows respectively.	20
15	Three functional forms of M variation comparison. They begin to exceed the M= 0.5 black line at Z=10, 7, 5 for linear, sinusoidal and square root respectively.	23
16	M28LinT1 versus M28SinT1 (Table 2). Secondary fault length comparison between linear and sinusoidal. Around 13 elements in length for sinusoidal compared to 11 elements for linear.	24
17	M28LinT1 versus M28SqrtT1 (Table 2) at 97 kyr. View from top of the model.	25
18	M28LinT1 versus M28SqrtT1 (Table 2) at 100 kyr. View from top of the model.	26
19	M57SinT2 versus M57SinT1 (Table 2). a) and b) are for M57SinT2, c) and d) are for M57SinT1.	27
20	M57SinT1 (Table 2) faulting and stress evolution with respect to time.	27

21	M57SinT2 (Table 2) faulting and stress evolution with respect to time.	28
22	M58SinT1 (Table 2) faulting and stress evolution with respect to time.	29
23	M58SinT2 (Table 2) faulting and stress evolution with respect to time.	31
24	M58SqrtT1 (Table 2) faulting and stress evolution with respect to time.	32
25	M58SqrtT2 (Table 2) faulting and stress evolution with respect to time.	33
26	M28SinT1 (Table 2) faulting and stress evolution with respect to time.	34
27	M57LinT1 (Table 2) faulting and stress evolution with respect to time.	36
28	M57SqrtT2 (Table 2) faulting and stress evolution with respect to time.	38
29	M28SqrtT1 (Table 2). Cut back behaviors in square root functional form model with different time.	42
30	M28SqrtT1 (Table 2). Square root functional form model at 160kyr. Pre-accumulated shear zone increase the shear force and cut the weak detachment front tip . .	43
31	M28SqrtT1 (Table 2). Bending stress drop in the crust close to dike due to cut back behavior.	44
32	M28SqrtT1 (Table 2). New fault front chase after initial abandoned breakaway. .	45
33	M28SqrtT1 (Table 2). Higher σ_{xx} in the median valley of conjugate plate at low M side.	46
34	Trade-off between change in bending force ΔF_b and weakening in the fault interface ΔF_w . H is the thickness of the brittle crust and γ is the size of ini- tial weak perturbation and A defines the maximum bending force change. (For more details, please refer to [Lavier et al., 2000])	47
35	Comparing nature observation at 13°N Mid-Atlantic Ridge to the Cut back behavior of model M28SqrtT1. The model topography is a mirror symetric flip according to the dash line, it reveals the case of M varies in a square root functional form from 0.2 to 0.8 to 0.2. For discussion on cut back formation mechanism, please refer to Section 4.2. The bathymetry is from GeoMapApp [Ryan et al., 2009].	50

1 Introduction

Around 70% area of the Earth's crust is the oceanic crust. New oceanic crust is constantly forming at the mid-ocean ridges (MORs), the longest mountain chains on the Earth. Seismic and volcanic activities are frequently happening along the MORs due to constantly seafloor spreading and magma upwelling. The interactions between the tectonics and magmatism along the MORs is considered to be the major contributing factor to the variation of the seafloor topography.

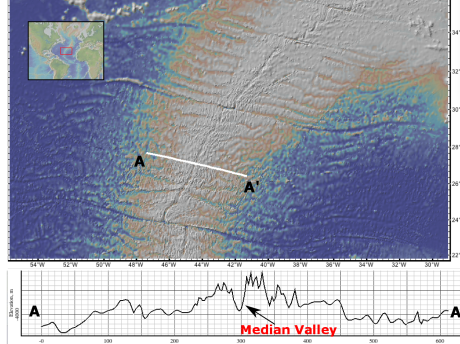
According to numerous high-resolution multi-beam bathymetry surveys, various characteristics of the topography along and across MORs are identified. How to explain the formation mechanisms of the observations has been an active research area. Two major questions have stimulated people's interests. First, what causes the distinct differences in axial topography between slow (median valley) and fast spreading ridges (axial high)? Second, for slow spreading ridges, why does topography from the center to tip of the ridge vary from high frequency symmetric abyssal hills to asymmetric long wavelength oceanic core complexes (OCCs)?

Geodynamic modeling along with a variety of geological, geophysical observation and lab experiment constraints have been used to study how does the interaction system between tectonics and magmatism at the MORs work under geological time scale.

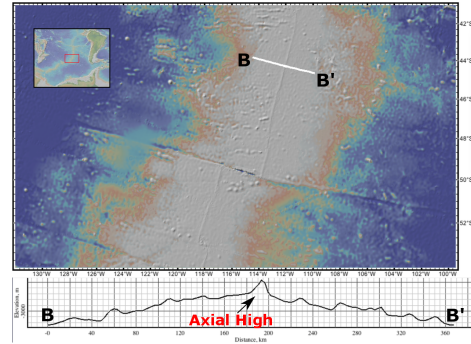
1.1 Review of Literature

According to [Fowler, 2004], variations in mid-ocean ridge morphologies are mainly controlled by four factors: magma supply, tectonic strain, hydrothermal circulation and spreading rate.
XT:Clarify the relationship between the four factors and try to cite the original work for each of them. (in Fowler2004, they didn't mention the ref for these four factors, page417 Chapter9.4.1) Among them, the spreading rate is the most important. Slow-to-intermediate spreading ridges (half spreading rate less than 4 cm/yr) produce median

valleys that are typically 10~20 km wide and 1~2 km deep (e.g., Mid-Atlantic Ridges, Figure 1(a)). Fast-spreading ridges (half spreading rate greater than 5 cm/yr) have axial highs that are 10~20 km wide, 0.3~0.5 km high (e.g., East Pacific Rise, Figure 1(b)).



(a) Slow spreading Mid-Atlantic Ridge



(b) Fast spreading East Pacific Rise

Figure 1: Profiles of bathymetry across MORs.

Slow spreading ridges exhibit along-axis variations as well in terms of the width and depth of median valleys, crustal thickness and the off-axis morphology. Figure 2 shows that the topographic profile nearer to the center of the ridge segment (A-A') is rather symmetric and has higher frequency. The maximum relief is about 1 km. In contrast, the near-tip profile (B-B') is asymmetric and has much lower frequency and a greater relief (~ 3 km). The bathymetry and crustal thickness along the ridge valley also varies. From [Chen and Lin, 1999], the maximum along-axis variation in crustal thickness ΔH_c is linearly increasing with segment length L, and the relationship is $\Delta H_c(L) = 0.0206L$ (Figure 3).

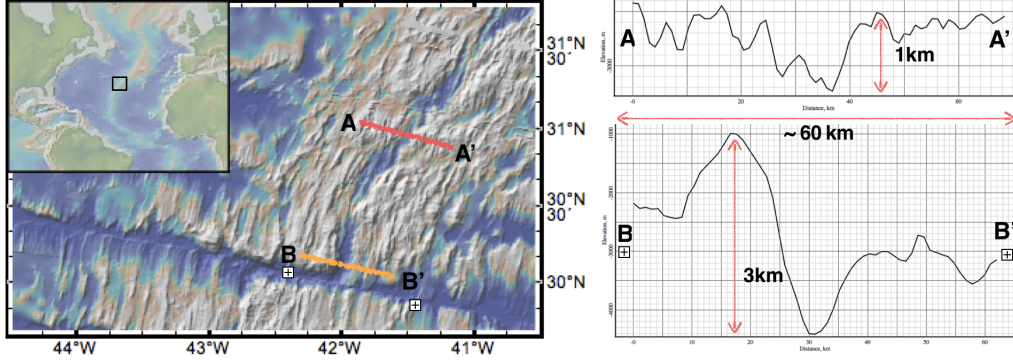


Figure 2: Two bathymetry cross-sections of Mid-Atlantic Ridge (MAR) with 10 times vertical exaggeration. A-A' is closer to the ridge segment center while B-B' is at the tip of the segment near the Atlantis Transform fault.

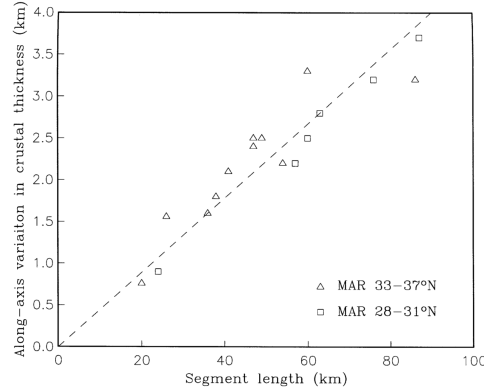


Figure 3: Relationship between the maximum crustal thickness variations (ΔH_c) along a ridge segment and the segment length (L). The dashed line is the best-fit linear regression of the combined data. [Chen and Lin, 1999]

Magma supply at MORs is mostly a passive process when no hot plume is present [Fowler, 2004]. Hot mantle rises up to fill the vacated room being created by plate separation and decompression leads to partial melting of the hot mantle. The melt upwells due to both pressure difference and buoyancy from lateral density difference. When the melt solidifies near the surface, it forms new crust. This diking process releases extensional stresses resulting from far-field forces (e.g. slab pull) that drive seafloor spreading.

The passive nature of magma supply results in the major difference between fast and slow spreading ridges in the amount of magma supply. At the fast spreading ridges, magma supply is always sufficient for accommodating plate separation by filling the space by

dikes. However, the amount of magma supplied in the form of dikes is not as much at the slow spreading ridges and the oceanic lithosphere experiences internal deformations (i.e. tectonics process like normal faulting) when the accumulated extensional stress exceeds the strength of the crust.

Buck et al. [2005] attributed the contrasting faulting patterns and ocean floor morphology of fast- and slow-spreading ridges to the difference in the amount of plate extension accommodated by diking. They defined the ratio between the rates of diking and plate separation as $M = V_{dx}/2V_x$, where V_{dx} is the extensional velocity of a widening dike and V_x is the half spreading rate of the MOR. According to this definition, $M = 1$ represents the case where magma supply is sufficient to release all the tensional stresses from plate separation. $M = 0$ corresponds to the case of no magma supply, in which diking does not account for any of the plate motion and therefore plates kinematics requires plates to go through internal deformations. As shown in Figure 4, an axial high forms at a fast spreading ridge ($M = 1$) due to buoyancy from lateral density difference across ridge axis but a median valley forms at a slow-spreading ridge ($M = 0.5$) due to near-axis normal faulting, which is in turn caused by the stretching of oceanic lithosphere.

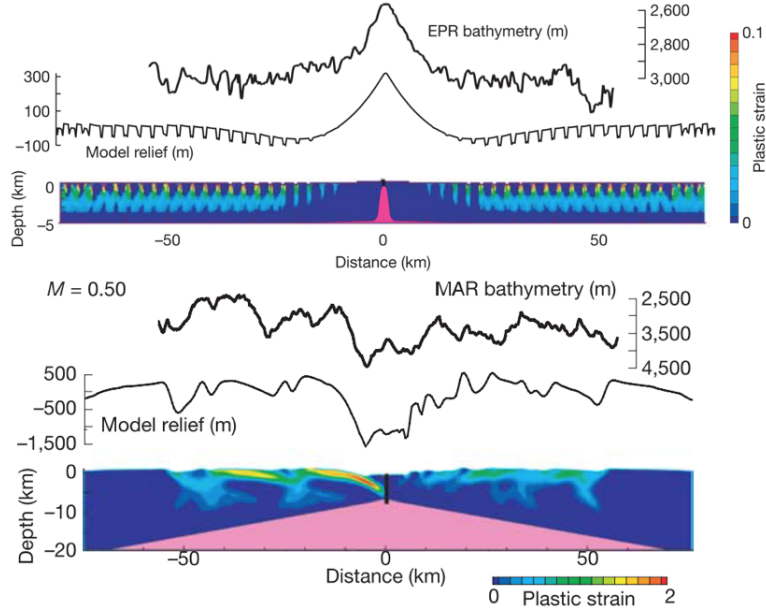


Figure 4: Upper one: modeling result for fast spreading agrees well with the observation of East Pacific Rise. Lower one: modeling result for slow spreading ridges agrees well with the bathymetry of Mid Atlantic Ridge. [Buck et al., 2005]

Tucholke et al. [2008] expand the investigation on the role of M in the mid-ocean ridge mechanics. They focus on the faulting behaviors of slow spreading ridges and find that the OCCs are most likely to form when M varies from 0.3 to 0.5. As shown in Figure 5, when $M = 0.7$, repeated diking pushes faults forming at the spreading center away from axis. Since the thickness of the brittle layer increases away from the ridge axis, frictional and bending energy for maintaining the fault also increases. When it exceeds the energy for breaking a new near-axis fault, the old fault will be replaced by the new one. When $M = 0.3 \sim 0.5$, the normal fault remains active for a long time and rotates to a very low angle normal fault (detachment fault), exhuming the lower crust and mantle materials to the seafloor. When M is less than 0.3, most of the tension is accommodated by intra-plate deformations rather than by diking and as a result, faulting pattern is more complicated and unsteady.

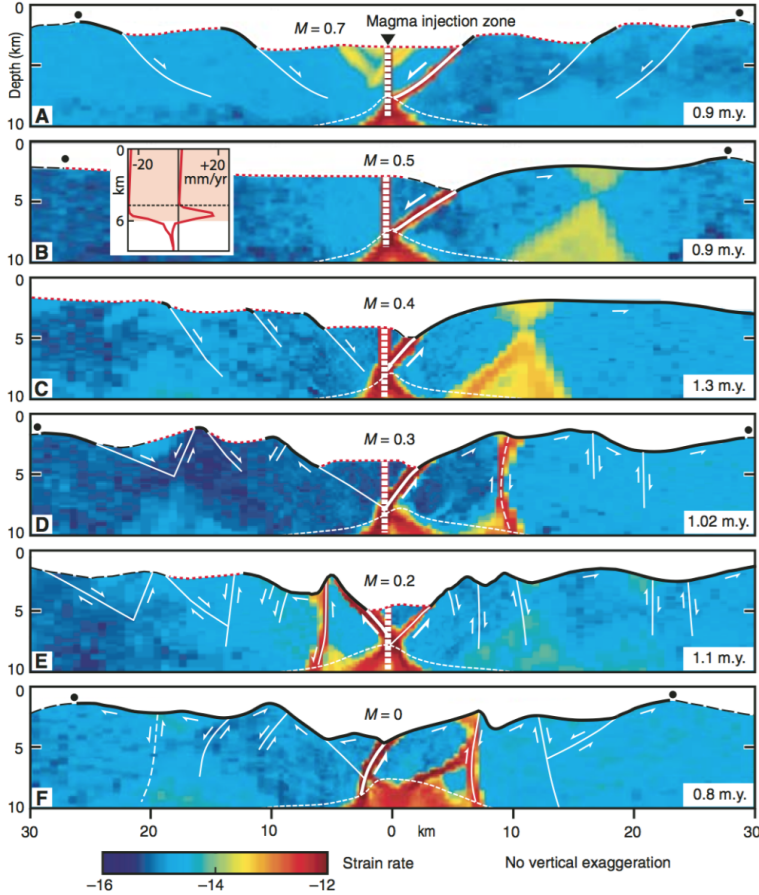


Figure 5: A~F: Faulting behaviors for different values of M . Geologic interpretation is superimposed on modeled distribution of strain rate. Dots show breakaways of initial faults. Dashed seafloor is original model seafloor, red dotted seafloor is formed dominantly by magmatic accretion, and solid bold is fault surface. Note that the detachment faults in B and C are not interrupted by secondary faults. [Tucholke et al., 2008]

1.2 Statement of Research Purpose

The M -factor formulation used in these previous 2D models successfully explained major features found in across-ridge profiles of seafloor bathymetry. However, 2D models have limitations in studying the along ridge-axis interactions, especially when important variables are not constant along the ridge axis. Magma supply at fast spreading ridges seems always sufficient for accommodating plate motions with little variation along the ridge axis. The relatively uniform topography along fast spreading ridges is considered to be consistent with the uniform abundance of the magma supply. However, along the slow spreading ridges, bathymetry, gravity anomaly and results from reflection and refraction seismology show strong correlation with variation in crustal thickness [Ryan et al., 2009, Chen and Lin, 1999, Lin et al., 1990, Tolstoy et al., 1993]. Because oceanic crust

is mainly formed by upwelled magma at the ridge, variation in the thickness of the crust implies variation in magma supply. At slow spreading ridges, the degree of cooling by hydrothermal circulation, thermal structures and even local spreading rate [Baines et al., 2008] also varies both along and across the ridge axis and they appear interrelated. Thus, for slow-to-intermediate spreading ridges, the interactions between tectonics and magmatism at MORs are inevitably 3D processes and 3D numerical models are desirable for better understanding factors controlling both across- and along-ridge topography variations.

The purpose of this thesis is to study how the along-ridge variation in M will make a contribution to the observed various topography assuming that M is the first order control over the topography evolution of MORs. In order to do so, we extend the M-factor formulation originally developed for 2D models to 3D by implementing it into a 3D numerical modeling code SNAC (StGermaiN Analysis of Continua) [Choi et al., 2008]. By systematically exploring the behaviors of the 3D models and comparing them with observations, we will be able to better understand how the mid-ocean ridge magmatism and tectonic deformations interact.

2 Methods

2.1 Method of approach

The numerical modeling code, SNAC, is an explicit Lagrangian finite element code that solves the force and energy ~~XT: find out which one is energy balance equation~~ balance equations for elasto-visco-plastic materials. Figure 6 shows major parts of the SNAC's algorithm.

For each time step of 0.5 yr, strain and strain rates are updated based on the initial or previous velocity fields under the constraints from boundary conditions. A constitutive model returns updated stresses corresponding to these deformation measures. Internal forces are then calculated from the updated stresses, which is plugged into the momentum balance equation together with the body force term. Then, the damped ~~XT: better understand the damped force~~ net force divided by inertial mass yields acceleration at a node point, which is time-integrated to velocity and displacement.

A 3D domain is discretized into hexahedral elements, each of which is in turn divided into two sets of tetrahedra. This symmetric discretization prevents faulting from favoring a specific direction or “mesh grains”.

Rheology for the oceanic lithosphere is assumed to be elasto-visco-plastic (EVP). When viscosity is high at low temperature, the rheology essentially becomes the Mohr-Coulomb plasticity with strain softening and thus can create shear bands that behave like faults. Strain softening is realized by cohesion decreasing with increasing amount of permanent (i.e., plastic) strain. I assume this relationship is linear for simplicity such that it is sufficient for a full description of strain weakening to define initial and final values of cohesion and a critical plastic strain at which cohesion becomes the final value. I define the rate of strain weakening as the cohesion difference divided by the critical plastic strain and use it as one of the model parameters. When temperature is high and viscosity is low, the rheology becomes the Maxwell viscoelasticity and can model creeping flow.

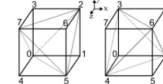
This property of the EVP model makes it possible to set up a structure with a brittle lithosphere and a ductile asthenosphere through a proper temperature distribution. Rheological parameters are taken from previous studies that use a similar rheology [e.g., [Buck et al., 2005](#); [Tucholke et al., 2008](#)] or from lab experiments [e.g., [Kirby and Kronenberg, 1987](#)].

For 3D diking processes, the expanding strain $\Delta\varepsilon_{xx}$ results from diking at the ridge leads to extra-stresses $\Delta\sigma_{xx}$, $\Delta\sigma_{yy}$ and $\Delta\sigma_{zz}$ in all three directions based on the linear elastic constitutive equations $\sigma_{ij} = \lambda\varepsilon_{kk}\delta_{ij} + 2\mu\varepsilon_{ij}$.

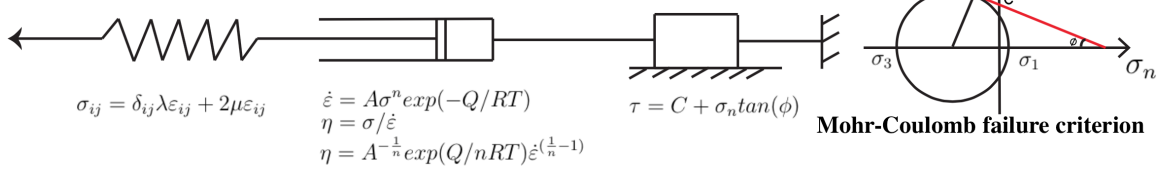
SNAC: a 3D, MPI parallelized, updated Lagrangian explicit finite difference code for modeling long-term tectonic evolution of the Earth's elasto-visco-plastic crust and mantle. (Choi et al., 2008)

Momentum Balance Equation: $\frac{\partial\sigma_{ij}}{\partial x_j} + \rho g_i = \rho \frac{Dv_i}{Dt}$

Spatial Decritization: A 3D domain is discretized into hexahedral elements, each of which is filled with two sets of 5 tetrahedra.



Elasto-Visco-Plastic (EVP) Rheology:



Diking M Formulation: $M = Vdx / 2Vx$ (Vdx is the dike accretion strain(dike widening) $\Delta\varepsilon_{xx}$ in each time step dt)

Stresses introduced by a dike accretion strain(dike widening) $\Delta\varepsilon_{xx}$ in each time step dt:

$$\Delta\sigma_{xx} = (\lambda + 2\mu)\Delta\varepsilon_{xx} \quad \Delta\sigma_{yy} = \lambda\Delta\varepsilon_{xx} \quad \Delta\sigma_{zz} = \lambda\Delta\varepsilon_{xx}$$

Figure 6: Essential components of the numerical method.

2.2 Model Setup

The 3D models has a geometry of $(60 \text{ km} \times 20 \text{ km} \times 20 \text{ km})$ in x , y and z axes respectively with a resolution of $\Delta x = 1 \text{ km}$ (Δx is the size of each hexahedron element). For comparison with the previous 2D models [e.g., [Buck et al., 2005](#); [Tucholke et al., 2008](#)], I also run pseudo-2D models and they have a geometry of $(60 \text{ km} \times 20 \text{ km} \times 1 \text{ km})$ in x , y and z axes respectively with a resolution of $\Delta x = 0.5 \text{ km}$. As shown in Figure 7, the initial temperature field linearly increases from 0°C at the top surface to 240°C at the depth of 6 km, reflecting enhanced cooling due to hydrothermal circulation. Below 6 km, the

temperature profile follows the semi-infinite half-space cooling model of moving plates [e.g., Turcotte and Schubert, 2002]. Two sides perpendicular to the z coordinate axis are free-slip. The top surface has vertical tractions from water columns, of which heights are locally determined as $(4000 - h(x, z))$ m, where $h(x, z)$ is the topography at a location, (x, z) . The bottom surface is supported by the Winkler foundation. Temperature is fixed at 0 °C on the top surface and at 1300 °C on the bottom surface. We adopt the power-law rheology of dry diabase [e.g., Kirby and Kronenberg, 1987, Buck et al., 2005].

For detail model parameters, please refer to Table 1.

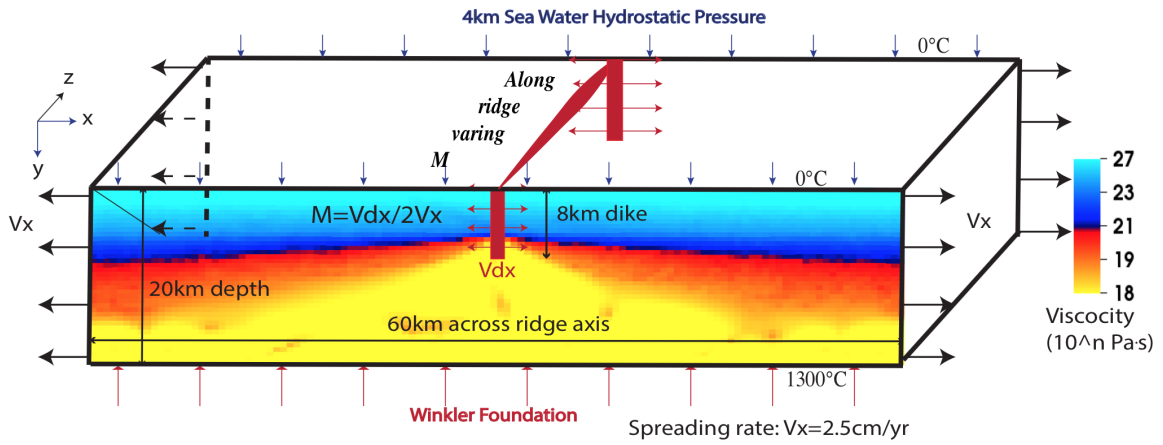


Figure 7: Model setup

2.3 Parameters to control

Before running 3D models, I have run hundreds of pseudo-2D models for initial setup and benchmarking with previous studies [e.g., Buck et al., 2005, Tucholke et al., 2008]. Preliminary pseudo-2D results show that the model behavior in faulting pattern is sensitive to the rate of strain weakening. Two cases of strain weakening are tested in the 3D models. In one case (denoted as Type 1 weakening), cohesion linearly decreases from 44 MPa (denoted as C_i) to 4 MPa (C_e) for plastic strain accumulating from 0 ($\varepsilon_{p_i}^1$) to 0.1 ($\varepsilon_{p_e}^1$). It has a characteristic fault slip of 150 m for pseudo-2D models and 300 m for 3D models. The other case (Type 2 weakening) assumes cohesion linearly decreasing from

44 MPa (C_i) to 4 MPa (C_e) for plastic strain accumulating from 0 ($\varepsilon_{p_i}^2$) to 0.33 ($\varepsilon_{p_e}^2$). In this case, the characteristic fault slip for pseudo-2D models is 500 m and for 3D models is 1 km. The characteristic fault slip is defined as $\Delta X_c = 3\Delta x \varepsilon_{p_e}$ where $3\Delta x$ represents the thickness of the shear bands which is usually 2 to 4 times Δx (size of a hexahedron element) [Lavier et al., 2000]. When ΔX_c amount of slip takes place at the fault interface, the cohesion of the material at the faulting interface decreases to C_e . In this way, under the same amount of ΔX_c , models with different resolution should produce the same faulting patterns.

Meanwhile, although how to estimate the M values from observations is a subject of on-going research, we do have constraints from a large dataset of bathymetry, gravity and seismic surveys as well as geological drilling. Generally, at slow spreading ridges, magma supplies mostly at the center of the ridge segment and decreases towards the tip of the segment [Tolstoy et al., 1993, Chen and Lin, 1999, Carbotte et al., 2015]. There is also evidence for shorter wavelength of 10 to 20 km discrete focus of magma accretion along the ridge axis [Lin et al., 1990]. Based on these constraints, I start considering a few scenarios of variations in M along the ridge axis. They are three M ranges (i.e. 0.2~0.8 (M28), 0.5~0.7 (M57) and 0.5~0.8 (M58)) with three simple functional forms of M variations (i.e. linear, sinusoidal and square root).

The numerical cost of a 3D model is non-trivial. For 2 Myr of model time, each model usually runs on 192 cores for about 48 hours (i.e., around 10^4 core-hours). Under this constraint of computational cost, I control only the following three parameters while fixing all the others: 1) three types of functional forms (i.e. linear, sinusoidal and square root); 2) three ranges of M variation along the ridge axis (0.5~0.7 (M57); 0.5~0.8 (M58); 0.2~0.8 (M28)) and 3) two types of weakening rate (Type 1 and Type 2).

Till now, $11 + 1$ 3D models are run (11 models with M varying along the ridge-axis and 1 model with constant M = 0.8. The complete list of 3D models is given in Table 2.

Table 1: Summary of 3D Model Parameters

Number	Variable	Description	Value	Units
1	W_{dike}	Dike width	2	km
2	D_{dike}	Dike depth	8	km
3	H	Crustal thickness at dike	6	km
4	dT/dy	Crustal thermal gradient	40	K/km
5	T_1	Temperature at lower boundary of crust	240	°C
6	g	Gravity acceleration	10	m/s ²
7	$demf$	Dimensionless force damping factor	0.8	N/A
8	dt	Time step	1.5768e+07	second
9	$topokappa$	Parameter for topography smoothing	0	N/A
10	$shadowDepth$	Ghost elements for parallel computing	2	N/A
11	$meshI$	Mesh number in X direction	60	N/A
12	$meshJ$	Mesh number in Y direction	20	N/A
13	$meshK$	Mesh number in Z direction	20	N/A
14	L_I	Length in X direction	20	km
15	L_J	Length in Y direction	20	km
16	L_K	Length in Z direction	20	km
17	ρ	Density	3000	kg/m ³
18	λ	Lamé's constant	30	Gpa
19	μ	Shear modulus	30	Gpa
20	$refvisc$	Reference viscosity	0.125e-17	Pa ⁻ⁿ /s
21	$activationE$	Activation Energy	276.0e+3	kJ/mol
22	vis_{min}	viscosity minimum cutoff	1.0e+18	Pa * s
23	vis_{max}	viscosity maximum cutoff	1.0e+27	Pa * s
24	$srexponent$	Power of power law in viscosity	3.05	N/A
25	$\varepsilon_{p_i}^1$	initial plastic strain for piecewise Type 1 weakening	0	N/A
26	$\varepsilon_{p_i}^2$	initial plastic strain for piecewise Type 2 weakening	0	N/A
27	$\varepsilon_{p_e}^1$	end plastic strain for piecewise Type 1 weakening	0.1	N/A
28	$\varepsilon_{p_e}^2$	end plastic strain for piecewise Type 2 weakening	0.33	N/A
29	C_i	initial Cohesion for piecewise weakening	44	Mpa
30	C_e	end Cohesion for piecewise weakening	4	Mpa
31	ϕ	Friction angle	30	°
32	$remesh_{timestep}$	Remesh when timestep reach its value	400000	N/A
33	$remesh_{length}$	Remesh when the global minimum of the ratio of the volume of a tetrahedron to one of its surface area	0.6	N/A
34	$topTemp$	Surface temperature	0	°C
35	$bottomTemp$	Bottom temperature	1300	°C
36	V_x	Half spreading rate	7.9e-10	m/s

Table 2: List of 3D numerical experiments.

Model	M range	Functional Form	Type of weakening	For short
1	M28	Linear	Type 1	M28LinT1
2	M28	Sinusoidal	Type 1	M28SinT1
3	M28	Square Root	Type 1	M28SqrtT1
4	M57	Linear	Type 1	M57LinT1
5	M57	Sinusoidal	Type 1	M57SinT1
6	M57	Sinusoidal	Type 2	M57SinT2
7	M57	Square Root	Type 2	M57SqrtT2
8	M58	Sinusoidal	Type 1	M58SinT1
9	M58	Sinusoidal	Type 2	M58SinT2
10	M58	Square Root	Type 1	M58SqrtT1
11	M58	Square Root	Type 2	M58SqrtT2
12	M88	Constant	Type 2	M88ConT2

3 Results

In this “Results” chapter, I first walk through the reference model (M28LinT1) and compare it with a constant M model (M88ConT2). Then, I describe in detail the major characteristics of the models. Finally, I compare the models in terms of 1) two types of the weakening rates; 2) three types of the ranges of M variation and 3) three types of the functional forms of M variation.

3.1 Reference model M28LinT1

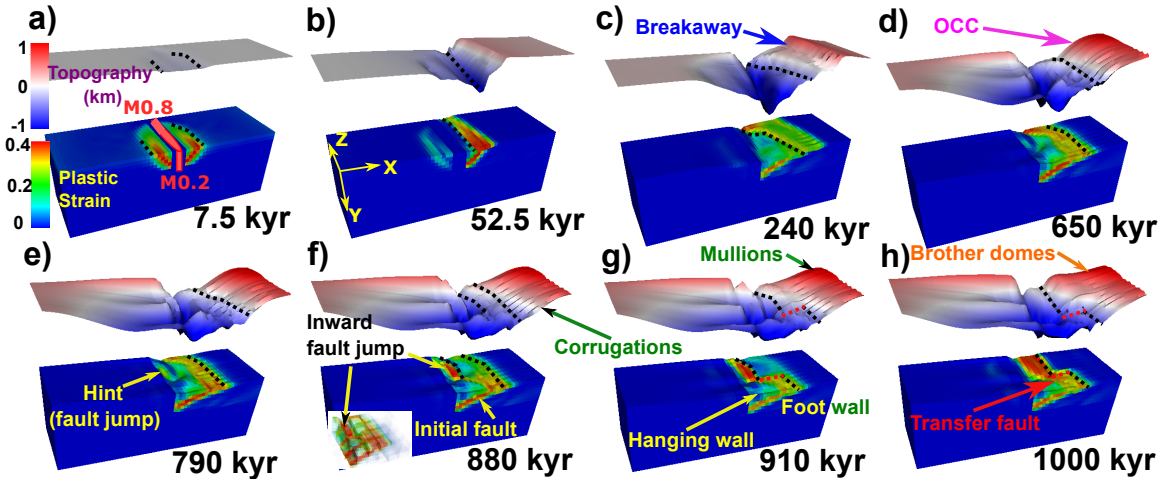


Figure 8: Evolution of plastic strain and surface topography of the reference model M28LinT1 (Table 2). Each snapshot shows plastic strain plotted on the model domain and the five times exaggerated topography. Initial seafloor is marked as a reference of 0 km of the topography. The bold dash lines (black) are the terminations of the detachment faults. The bold dash lines (red) in g and h are the transfer faults that connect the terminations along the ridge. The inset in f plots plastic strain with opacity linearly proportional to its value.

I consider the model with M varies linearly from 0.2 to 0.8 along the ridge axis with type 1 weakening rate (M28LinT1) as our reference model. The major characteristics of the model are indicated in the Figure 8. They are breakaway (Figure 8.c); oceanic core complex (OCC) (Figure 8.d); terminations of the detachment faults where the active faulting interfaces reache the seafloor (Figure 8.e); new high angle normal faults forming near

the ridge axis, termed as “inward fault jump”; corrugations (Figure 8.f) and mullion structures (Figure 8.g); and the side-by-side “brother domes” (Figure 8.h).

As shown in Figure 8, the model creates a median valley that widens and deepens with increasing plate extension (Figure 8.a.b.c). The rate of its widening and deepening at a specific location along the ridge is inversely proportional to the M value (i.e. rate of local magma supply).

For the first 7.5 kyr (Figure 8.a), normal faults (represented by localized plastic strain) begin to form near the ridge axis. Because stresses due to plate motions accumulate faster at the lower M side than at the higher M side, faults initiate at the lower M side first and then propagate to the higher M side.

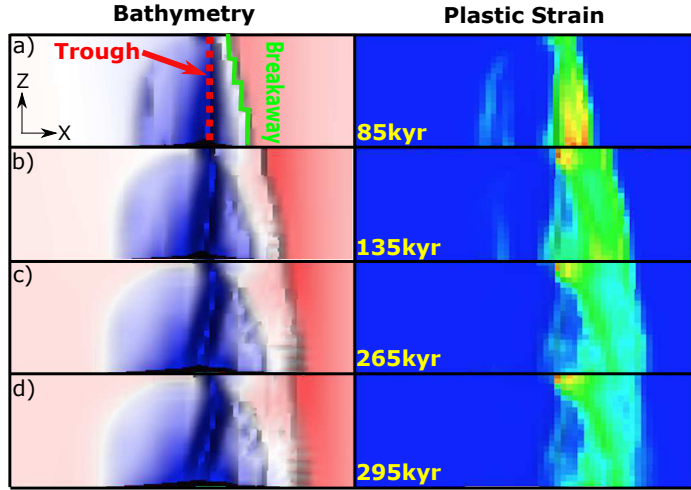


Figure 9: Bird’s-eye view of the evolution of breakaway (marked by green bold line) and depressed narrow zone along the ridge axis (“trough”) (red dash line in (a)) for model M28LinT1 (Table 2). This figure share the same color scales with Figure 8.

By 52.5 kyr (Figure 8.b), the normal fault on the right hand side of the ridge axis continues to evolve while the one on the left becomes inactive. The choice of which fault to develop seems to be made due to a small numerical perturbation between the two faults seen in Figure 8.a although the model setup is symmetrical across the ridge axis. The timing difference of initiation of faulting along the ridge axis creates an offset in the x -axis direction between the breakaways along the ridge that the breakaway at the lower M side

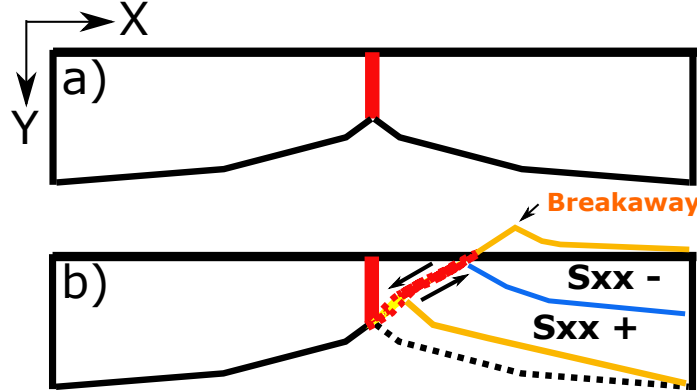


Figure 10: Bending stress illustration. The blue line is the neutral plane where $\sigma_{xx} = 0$. Above the neutral plane is compression ($\sigma_{xx} < 0$) and beneath it is tension ($\sigma_{xx} > 0$).

extends further than that of the higher M side (Figure 9). The offset is maintained because the extending velocity of the breakaways to move away from the ridge axis is controlled by the far field extension rate, V_x . The plastic strain also shows similar along ridge offset in x -axis direction. However, the along ridge offset in x -direction of the tips of the extending plastic strain reduces at ~ 295 kyr (Figure 9.d) because once the detachment fault at the lower M side bends to its lowest dip angle, the termination of the detachment fault stops extending and the healing effect implemented in the model reduces quickly the plastic strain of the inactive fault interface that has been exhumed to the seafloor. While at the higher M side, the termination keeps extending and reduces the initial offset generated by the asynchronous initiation of faulting. In addition, as the fault slips, crust at the footwall bends in a clockwise rotation as illustrated by Figure 10.

By 240 kyr (Figure 8.c), the median valley further deepens and widens. The detachment fault keeps slipping and as it bends, the termination at the lower M side ($M < 0.3$) extends ~ 15 km away from the ridge axis with the dip angle decreases to $\sim 30^\circ$ at the root of the fault and to $\sim 0^\circ$ at the exposed fault interface. However, for the detachment at the higher M side (especially for $M > 0.7$), the dip angle remains high and the termination of the detachment is closer to the ridge axis. The maximum relief between the breakaway and the depressed narrow zone (trough) inside the median valley becomes larger than 1 km. In addition, ~ 1 km wavelength corrugations begin to show up between the break-

away and termination at the lower M side ($M < 0.3$). The wavelength of the corrugations is relatively more regular than the mullion structures (Figure 8.g) because they share different formation mechanism as will be described in the following sections. The trough evolves from a straight line parallel to the ridge axis (Figure 9.a) to a line oblique to the ridge axis and the obliquity increases with extension (Figure 9.b,c,d).

By 650 kyr (Figure 8.d), the median valley becomes wider and deeper. The detachment fault reaches its lowest dip angle and its termination stops extending. The break-away already moved out of the model domain. The fault slip is already larger than the thickness of the crust and the upper mantle materials are exhumed to the surface. The previous fault interface bends over and dips away from the ridge axis, producing a cylindrical OCC. A hint of the inward fault jump shows up at the higher M side ($0.5 < M < 0.65$).

By 790 kyr (Figure 8.e), the hint of the inward fault jump evolves and propagates toward the higher M side ($M > 0.5$). However, the initial detachment fault is still active and takes up most of the extension. The distance between the termination of the detachment fault and the ridge axis varies along the ridge that the termination at the lower M side is further away from the ridge axis.

By 880 kyr (Figure 8.f), at the higher M side ($M > 0.5$), the hint of the inward fault jump evolves to a high angle normal fault that cut through the higher M side ($M > 0.5$) and coexists with the initial detachment fault (shown in the inset).

By 910 kyr (Figure 8.g), the inward fault jump takes up all the extension at the higher M side ($M > 0.5$) and substitutes the initial detachment fault. At the higher M side, previous hanging wall becomes footwall and moves with the spreading plate to the positive x -axis direction, however, at the lower M side, due to the limited magma supply, the hanging wall follows the conjugate plate and moves toward the negative x -axis direction (Figure 11). This opposite directions of velocities result in a dextral shear stress σ_{xz} region at the lower M side ($M < 0.5$) $\sim 45^\circ$ oblique to the ridge axis (Figure 12) and it produces a new trough inside the median valley that aligns with it. Combined with the previous

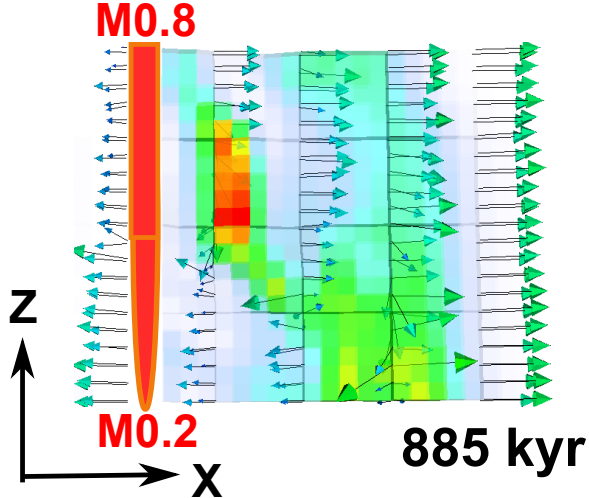


Figure 11: Bird's-eye view of velocity field with plastic strain plotted with opacity linearly proportional to its value. (color scale the same as Figure 8.a))

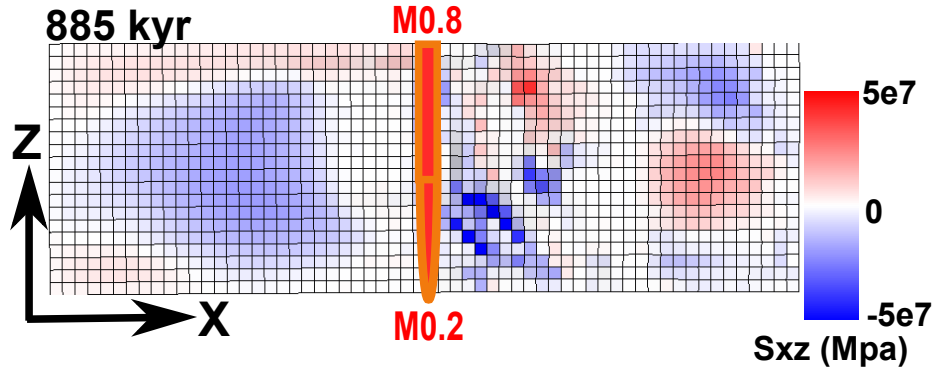


Figure 12: Bird's-eye view of σ_{xz} .

trough, an “X” shape topography low is created in the model.

3.1.1 Constant M along the ridge axis (M88ConT2 Table 2)

As a comparison to the varying M models, a constant M model is run.

As shown in Figure 13, model M88ConT2 produces a ~ 20 km wide and $1\sim 2$ km deep median valley. It is similar to the generally observation of the Mid-Atlantic Ridges. The width and depth of the median valley is almost constant along the ridge axis as contrast to the varying M models. The variations along the ridge axis in breakaway, termination as well as the corrugation mentioned in the reference model (M28LinT1) are not produced.

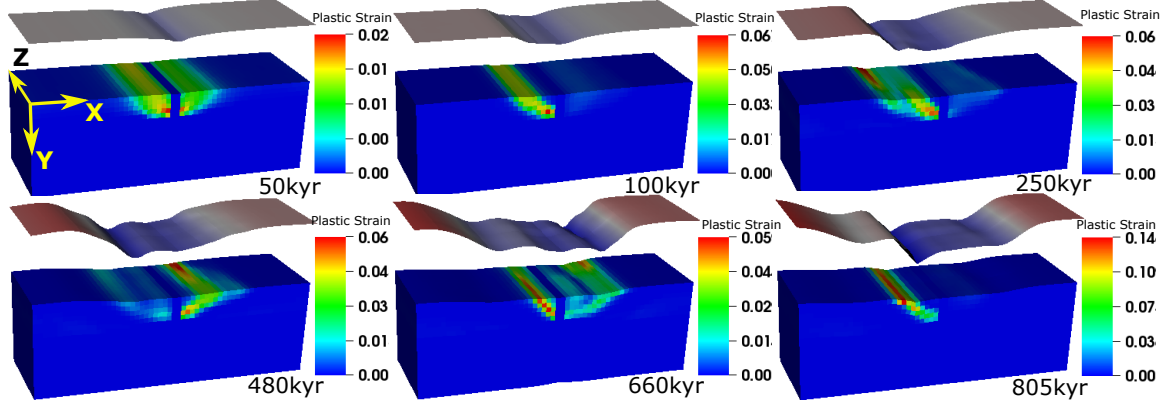


Figure 13: Evolution of plastic strain and surface topography of the model: M88ConT2 (Table 2).

Because the magma supply is constant along the ridge with $M = 0.8$, there is no along ridge axis variation in the rate of tensional stress accumulation. Thus, the normal faults along the ridge initiate at the same time and the slipping rate of the fault is also constant along the ridge axis. The synchronized fault initiation results in no offset between breakaways and the constant slipping rate produces no along ridge axis variation in the position of the termination. Thus, neither corrugations, mullion structures nor along ridge axis variation in width and depth of the median valley are generated.

Normal faults alternate on each side of the ridge axis with a period of ~ 300 kyr due to the mechanism mentioned in the “Introduction” section for the 2D models of $M > 0.5$. This fault alternation produces the symmetrical high frequency abyssal hills. For 3D models, why and how fault alternates on each side of the ridge axis is slightly different than the previous 2D studies. It will be further described in the following section.

3.2 Main characteristics of the models

Six main characteristics of the models are described in this section. They are “location of the termination”, “geometry of the trough inside the median valley”, “second fault”, “fault alternation”, “cut-back” and “corrugations”.

3.2.1 Location of termination

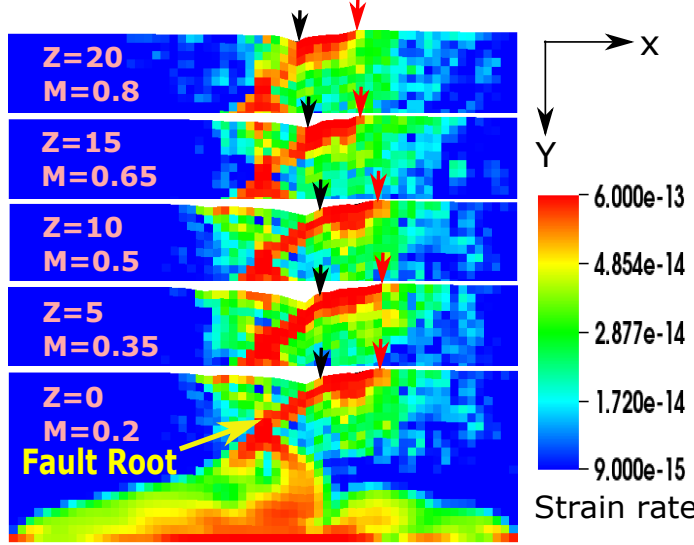


Figure 14: Five slices of strain rate along the ridge axis for the model M28LinT1 (Table 2) at 107.5 kyr. The 5 terminations and 5 breakaways along the ridge axis are marked by the 5 black and 5 red arrows respectively.

The location of the termination (bold dash line in Figure 8.c.e)) of the detachment fault where footwall begins to be exhumed to the seafloor varies along the ridge axis. As shown in Figure 14, the highest strain rate regions (red) can be interpreted as the active detachment fault interfaces. When $M \leq 0.5$, although the rate of fault slip should be higher for lower M , the rate of bending of the hanging wall or the rate of decreasing in the dip angle of the detachment fault has a maximum value that corresponds to the far field extension rate V_x . Because for $M < 0.5$ (Figure 14, ($M = 0.2, 0.35, 0.5$)), the detachment fault roots at the same place (marked in the slice of $M = 0.2$) at the intersection between the center dike and the brittle-ductile transition (BDT), the amount of bending in the footwall of the detachment fault is determined by how far the termination extends away from the ridge axis. In other words, in order to spend least frictional energy during faulting, the detachment fault interface between the two ends (termination and root) tends to be a straight line. Thus, the dip angle of the fault is inverse proportional to the distance between the termination and the root of the normal fault when $M < 0.5$. So the farther the

distance between the termination and the root of the fault, the lower its dip angle. Since the breakaways at the lower M side ($M < 0.5$) moves with the extending plate under the same velocity V_x , and the initiation time difference of the normal faults at the lower M side is similar (Figure 8.a), the distances between the breakaways and the roots of the faults are the same. Meanwhile, the distance between breakaways and terminations as indicated by the red and black arrows in the Figure 14 is similar along the ridge axis. Thus the dip angles of the faults at the same time along the ridge-axis are very much the same. However, when $M > 0.5$ (Figure 14, (M = 0.65, 0.8)), the amount of fault slip decreases as M increases. The crust at the footwall experiences less bending and the detachment fault remains in a higher angle as well as that the terminations are closer to the ridge axis. Because the root of the fault is slowly pushed away from ridge axis while the breakaways of the faults are closer to ridge axis due to a later initiation of the fault. In addition, the crust thickness that the fault cuts through is slowly increasing as the fault being pushed away from ridge center due to excessive diking. These three factors together contribute to a higher dip angle. In a unit time, the volume of the exhumation is also smaller for the higher M side. One thing needs to be noted is that the trough at the higher M side correspond to the terminations but detached from the terminations at the low M side ($M < 0.5$) as shown in Figure 14.

3.2.2 Geometry of the trough inside the median valley

The trough inside the median valley evolves from a straight line parallel to the ridge-axis (Figure 9.a) to a line oblique to the ridge-axis (Figure 9.b,c,d) for model M28LinT1. Initially, the trough corresponds to the termination of the detachment fault. Due to the coupling along the ridge axis, fault propagates from front to back in almost a straight line parallel to the ridge axis. However, as the detachment fault bends at the lower M side, the trough is detached from the termination and due to lower magma supply, the trough at the lower M side is pulled to the conjugate plate to the negative x -axis direction. While

the trough at the higher M side ($M > 0.5$) are pushed away from the ridge axis. However, since the trough cannot bypass the termination, the trough at $M = 0.8$ is restricted at the termination. Together it generates the curved trough (Figure 9.b,d).

3.2.3 Second fault

The second fault is another common characteristic of the models. As shown in Figure 8, at the region with $M > 0.5$, the existing normal fault is pushed away from the ridge-axis due to excessive diking. As it moves away from the ridge axis, the frictional energy for the fault, the bending energy for the foot wall as well as the gravity that resists the exhumation of the foot wall increase until the sum of the energy reach an upper limit that breaking a new fault near the ridge axis causes less energy, another new near ridge axis normal fault is produced. As it evolves, the initial detachment fault becomes inactive. This new produced near ridge axis high angle normal fault is termed as the “second fault”. Compared to fault alternation, it forms at the same side of the ridge axis and its length is consistent with the region along the ridge axis where $M > 0.5$ rather than cut through the whole MOR segment. As the second fault evolves, it connects to the initial detachment at the lower M side ($M < 0.5$) and generates a curved termination along the ridge.

3.2.4 Fault alternation

3.2.5 Cut-back

3.2.6 Corrugations

Corrugations due to anastomosing

Corrugations due to asynchronous normal faulting

3.3 Effects of the functional forms of M variation

As shown in the ~~EC:~~tables [which table? Specify.], ~~EC:~~the models with ~~EC:~~M28 [Before starting to use this notation, define and explain it first!] with type 1 weakening is ~~EC:~~the only M range that has three functional forms data points available [This sentence gives an impression that you didn't want to use these three but had no choice but to. This is not the case, I believe. Probably you'd want to point out that one of these three is the reference model that has been fully described earlier. So, we are in a better position to compare it with similar models with different functional forms. In fact, I think this introductory sentence can be thrown out.]

~~EC:~~There are two phenomena that show distinct differences with respect to different functional forms. By comparing M28LinT1 with M28SinT1 and M28sqrtT1, I identified two main characteristics in the different behaviors of these models due to different functional forms of M variation. One is the geometry and timing of the secondary fault. The other is the “Cut back” behavior. ~~EC:~~mostly observed in the square root model. [No need to spill the beans.]

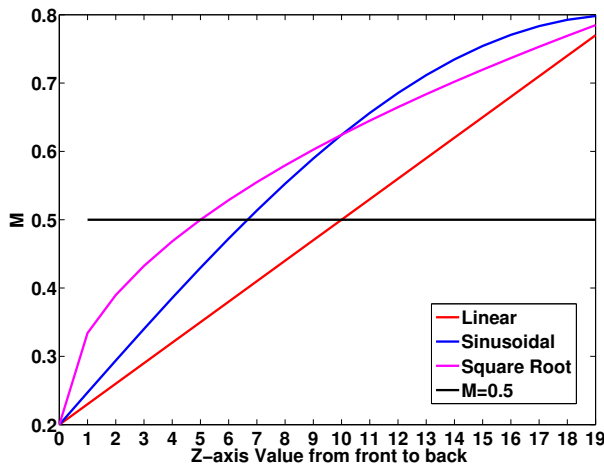


Figure 15: Three functional forms of M variation comparison. They begin to exceed the $M = 0.5$ black line at $Z = 10, 7, 5$ for linear, sinusoidal and square root respectively.

Second Fault For the linear functional form, the second fault ^{XT}: [add a definition of secondary fault in the begining, here add a link of figure about primary and sec fault, enlarge the second fault and add label in the figure and use it here] at the high M side has started accommodating most of the extension at around 900 kyr and the initial detachment becomes inactive ^{XT}: [(Figure 16)]refer to Figure 8.f is better. It nucleates from the ridge center where $M = 0.5$ and then propagates to the $M = 0.8$ end.

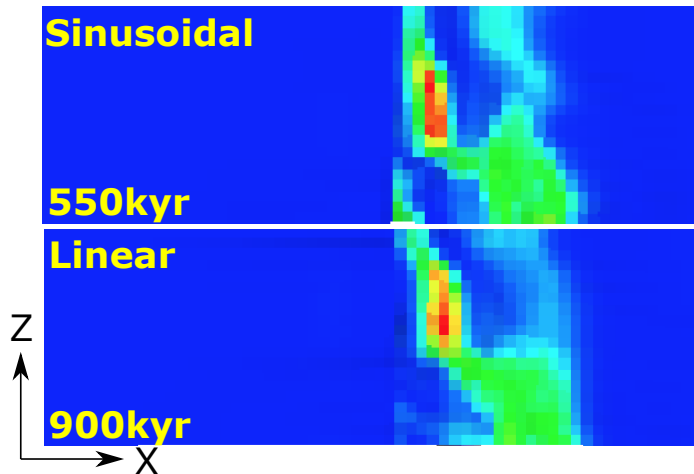


Figure 16: M28LinT1 versus M28SinT1 (Table 2). Secondary fault length comparison between linear and sinusoidal. Around 13 elements in length for sinusoidal compared to 11 elements for linear.

For the sinusoidal form, the second fault begins to form at a much earlier time around 550 kyr (Figure 16). The sinusoidal form consistently has higher M values than the linear form (Fig. 10), implying a greater amount of magma supply. The first forming fault moves away from the ridge axis faster and locks earlier in the case of the sinusoidal form. As a result, the second fault appears earlier than in the case of the linear M variation. In addition, the sinusoidal form produces the second fault with a greater along-strike dimension than the linear form because this length is proportional to the length of the $M \geq 0.5$ portion of the ridge (Figure 15). For square root, there is no secondary fault forming because the “cut back” behavior releases the tensional stress in the hanging wall.

Cut-back ^{XT}: [Define a cut-back and think about a different name.] The cut-back char-

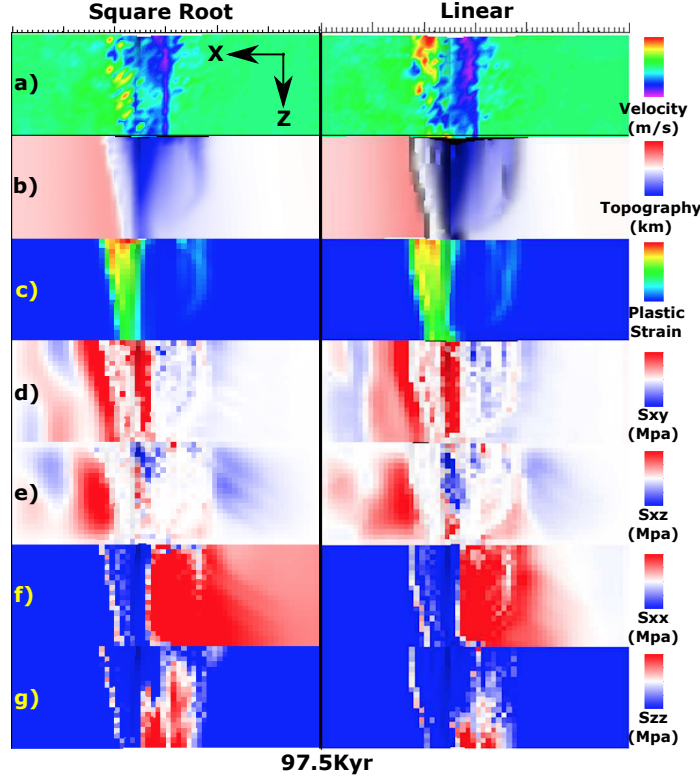


Figure 17: M28LinT1 versus M28SqrtT1 (Table 2) at 97 kyr. View from top of the model.

acterizes but are not limited to the models with the square root form of M variation.^{XT:} [exclusively about the square root models?] As shown in Figure 17, Figure 18 and Figure 29^{XT:} [Bring up Fig. 26 here and include only the cut-back panel.], between 97.5 kyr and 100 kyr, there are cut-backs in the square root model M28SqrtT1 at the low M side where hanging walls with surface area of $\sim 60 \text{ km}^2$ and $\sim 120 \text{ km}^2$ (the red block) suddenly rebound backwards towards the ridge axis as seen in 100 kyr and 160 kyr (Figure 18.a and Figure 29.d,e,f), along with sudden topography drop (Figure 29.d,e 2nd row), σ_{xy} and σ_{xz} released, termination falls back (Figure 29.f 3rd row).

3.4 Effects of the weakening rate

According to our available twelve 3D models, we have three pairs of models that both have type 1 and type 2^{XT:} [might want to add a ref to the section defining these.] weakening while the range of M and functional form are maintained to be the same. They are

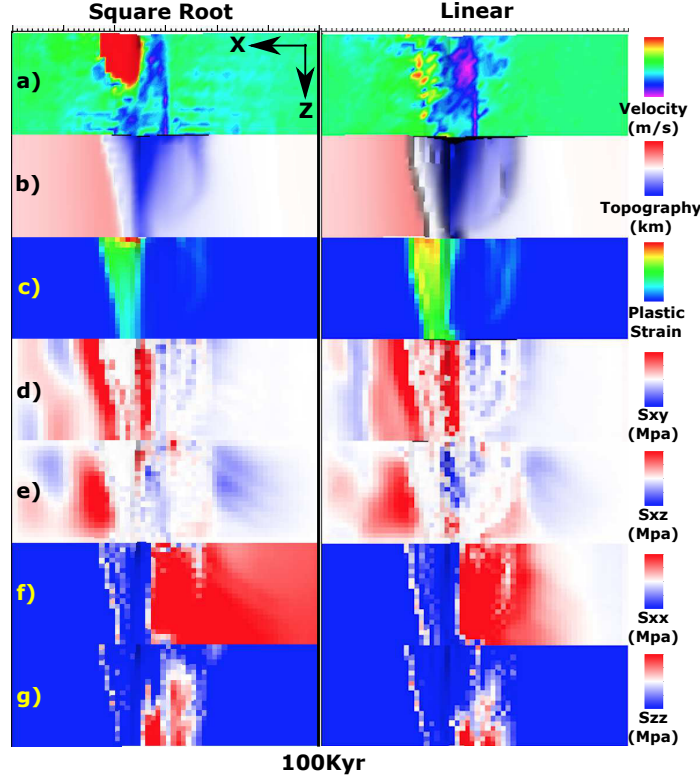


Figure 18: M28LinT1 versus M28SqrtT1 (Table 2) at 100 kyr. View from top of the model.

M57SinT1/T2, M58SinT1/T2 and M58SqrtT1/T2.

M57SinT1 versus M57SinT2 Initially, both models develop normal faults on both sides of the ridge axis^{XT: [no hyphen in “ridge axis”.]} at the low M side. In the model with the faster weakening rate (M57SinT1), faults propagate toward the high M side and cut through the whole crust by 25 kyr but this process completes later at 50 kyr in the model with the slower weakening rate (M57SinT2). At around 310 kyr, the second fault appears at the high M side^{XT: [instead of z=5, use a M value.]} of M57SinT2 while where $M \leq 5$ [some M value], the initial fault remains active (Figure 19.a) and b)). However, when the weakening is fast (M57SinT1), cut-back happens at around 260 kyr and help to maintain a high angle fault with closer to ridge axis termination. The initial fault remains, no secondary fault forming (Figure 19.a) and b)). In addition, the width of median valley at low M side is wider for M57SinT2 than M57SinT1 (Figure 19.a) and b) versus c) and

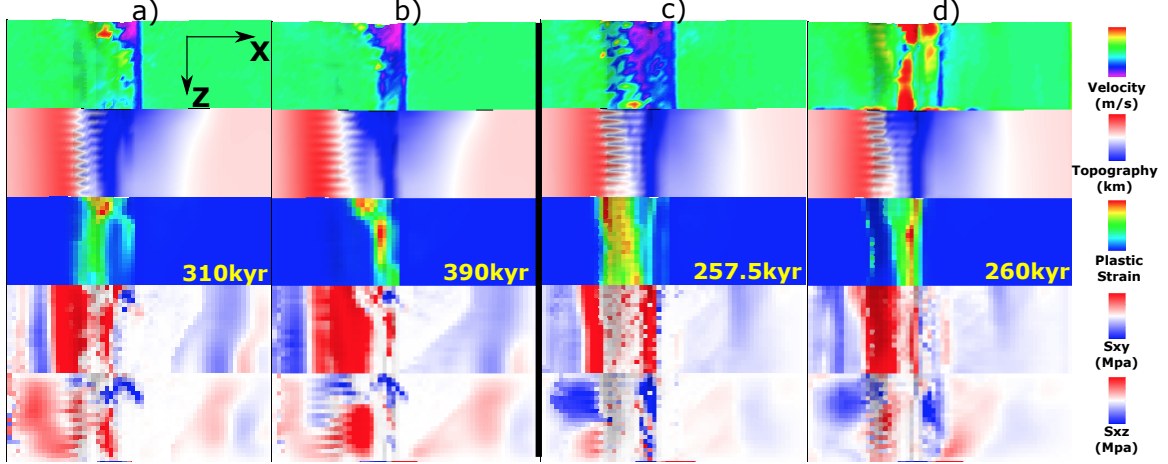


Figure 19: M57SinT2 versus M57SinT1 (Table 2). a) and b) are for M57SinT2, c) and d) are for M57SinT1.

d)) due to slower weakening (type 2) allows a more distributed tensional stress σ_{xx} rather than fast weakening that once a fault is established, larger amount of tensional stress σ_{xx} will be released at the fault.

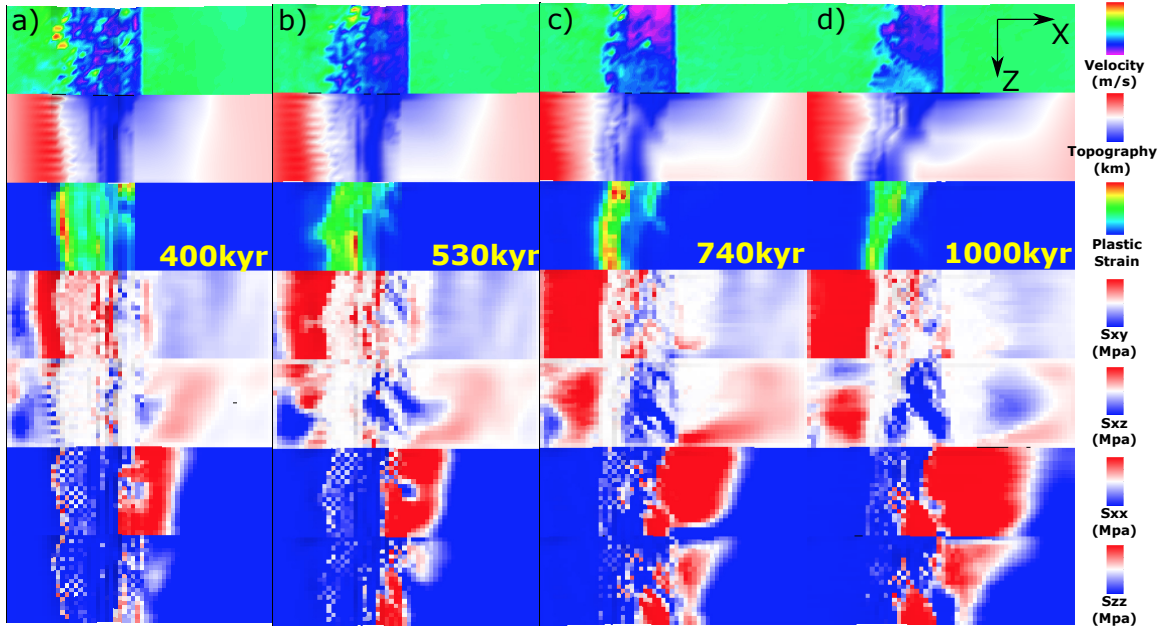


Figure 20: M57SinT1 (Table 2) faulting and stress evolution with respect to time.

M57SinT1 For M57SinT1, as shown in Figure 20, at 400 kyr (Figure 20.a), there is an antithetic fault forming at the low M side accommodating part of the extension, which re-

sults in a curved termination at the far frontier. As it evolve (530 kyr (Figure 20.b)), the termination at the low M side further recedes backward while the termination at the center ($Z = 11 \sim 13$) extends further. This curved termination leads to a curved topography (white curve in the second row). As the fault evolves and bends further away from the axis, at the time of 740 kyr, another antithetic fault forming again at the low M side (Figure 20.c). It doesn't take the place of initial fault and disappear soon, however, it again releases tensional stress and results in that the termination at far front recedes backward. At 1000 kyr (Figure 20.d), an Atlantiss Massif shape OCC is produced (low M side (lower magma supply) has a wider dome and high M side (higher magma supply) has a narrower dome) due to the along ridge axis termination evolution. Corrugations with wavelength varying from hundreds to kilometers are also created.

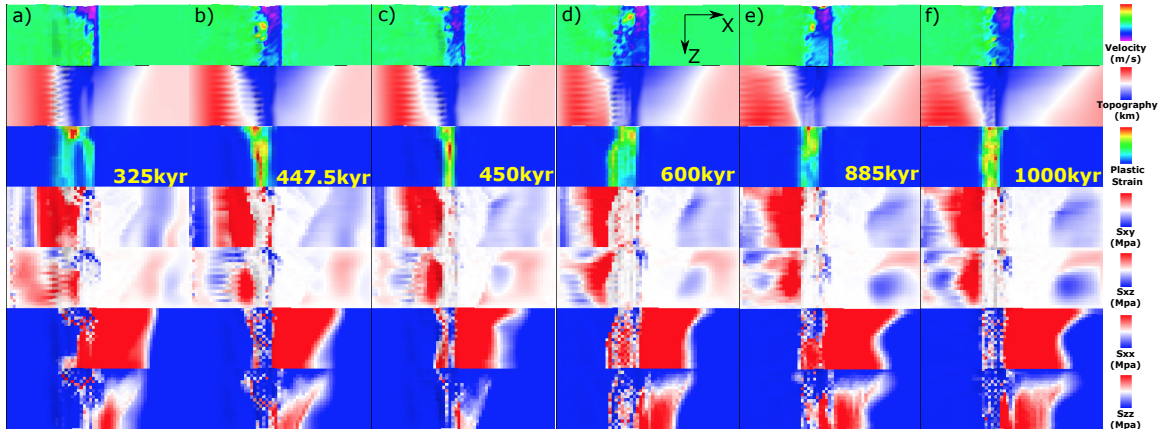


Figure 21: M57SinT2 (Table 2) faulting and stress evolution with respect to time.

M57SinT2 For M57SinT2, as shown in Figure 21, instead of maintaining one fault all the time for M57SinT1, it creates secondary fault at high M side with different mechanism several times. A secondary fault is created at 325 kyr (Figure 21.a), when a new near axis normal fault take the place of the initial one at high M side. Between 447.5 kyr (Figure 21.b) and 450 kyr (Figure 21.c), termination falls back, and as it evolve, termination at the high M side extends further at 600 kyr (Figure 21.d). At 885 kyr (Figure 21.e), a secondary fault propagates from low Z to high Z and terminates the further extended fault at

high Z and maintain a near ridge axis termination.

3.4.1 M58SinT1 versus M58SinT2

A major difference between M58SinT1 and M58SinT2 is that M58SinT1 keep faulting at one side of the ridge axis while M58SinT2's fault alternates.

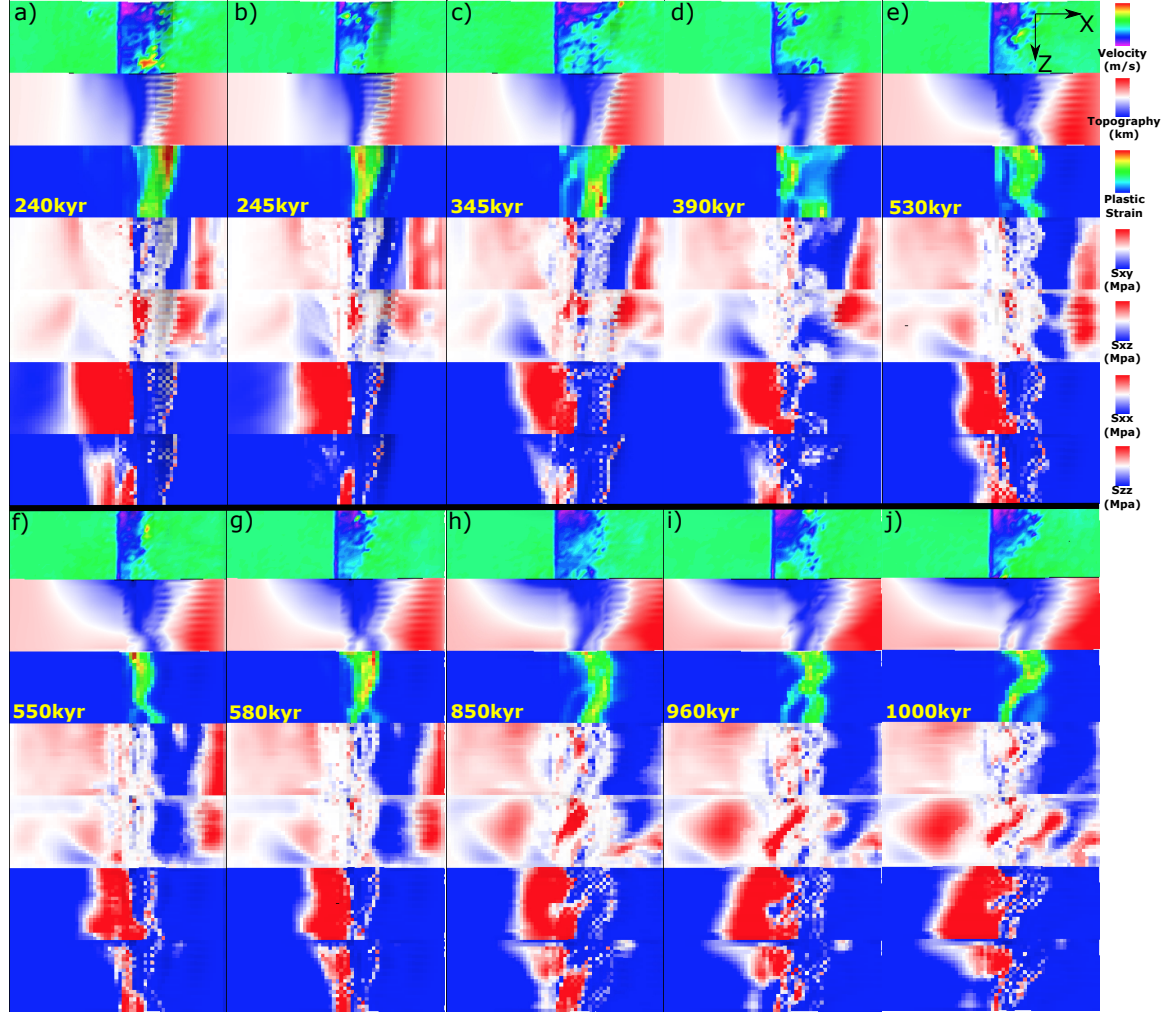


Figure 22: M58SinT1 (Table 2) faulting and stress evolution with respect to time.

M58SinT1 As shown in Figure 22, in 1Myr, the fault keeps on the right hand side of the ridge axis. It evolves dynamically. Between 240 kyr (Figure 22.a) and 245 kyr (Figure 22.b), there is a cut back. At 345 kyr (Figure 22.c), at low Z side, there are two offset antithetic faults ($Z=1 \sim 2$ and $Z=5 \sim 9$) in the hanging wall begin to evolve and

soon connect to each other forming anastomosing fault zone. At 390 kyr (Figure 22.d), the new near axis anastomosing fault zone replace the old further away from ridge axis detachment. There is dextral σ_{xz} forming on the right hand side of the new anastomosing fault zone ((Figure 22.d), row 5) due to the offset between the new near axis fault at low Z side and extended further fault at high Z side and leads to the development of a $\sim 45^\circ$ shear zone connection between the new near axis fault zone at low Z side and the further away from axis original detachment at high Z side. It also creates a curved termination which will lead to a curved topography (boundary between blue and white) seen at 530 kyr (Figure 22.e). Note that this curved termination can be a mechanism for producing large wavelength (several kilometers) undulating corrugations. Between 530 kyr (Figure 22.e) and 550 kyr (Figure 22.f), there is another cut back happens. Terminations fall backwards to near ridge axis position. At 580 kyr (Figure 22.g), at the high Z side, a new near ridge-axis high angle normal fault begin to initiate under the assistance of rotational force from low Z side due to along ridge axis coupling. This produces a large rider block with several kilometers in its length scale. Previous “S” curved termination now evolves to a half circle curve and it soon affects the curve of topography as seen at 850 kyr (Figure 22.h). Due to along ridge axis variation in diking, a large sinistral shear zone (red region $\sim 40^\circ$ oblique to ridge axis seen in 5th row of 960 kyr (Figure 22.i)) keep developing and cut the circle curved fault zone at 850 kyr (Figure 22.h) into a new fault zone with higher curvature as seen in 1000 kyr (Figure 22.j).

M58SinT2 As shown in Figure 23, the fault initiates on the left hand side of the ridge axis (Figure 23.a). Low Z side extends further than high Z side. It takes around 100 kyr to form into a localized fault plane due to slower rate of weakening. At 215 kyr (Figure 23.b), another fault on the conjugate plate begin to evolve and replaces the initial one. As seen from (Figure 23.b), corrugations are created at low Z side. At 330 kyr, a third fault forming at the left hand side of the ridge axis. Between 490 kyr (Figure 23.d) and

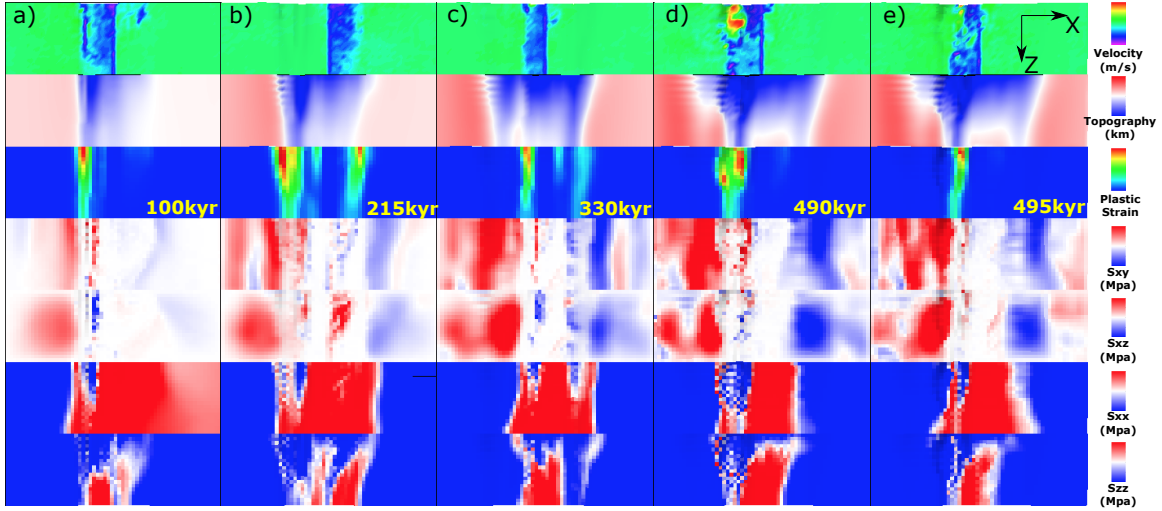


Figure 23: M58SinT2 (Table 2) faulting and stress evolution with respect to time.

495 kyr (Figure 23.e), there is a cut back.

3.4.2 M58SqrtT1 versus M58SqrtT2

The major difference between M58SqrtT1 and M58SqrtT2 is also whether the normal fault alternates or not.

M58SqrtT1 As shown in Figure 24, initially, there is a 5 element offset between breakaways along the ridge axis due to along ridge axis variation in diking (Figure 24.a). At 370 kyr (Figure 24.b), there is a vertical tensile failure at $Z= 1 \sim 2$. Two parallel dextral (blue) shear regions are seen (5th row). The low Z shear zone assists in the shear failure observed at 400 kyr (Figure 24.c), and it develops into near ridge axis normal fault ($Z=4 \sim 12$) and propagates to high Z side which eventually cuts through and reaches $Z= 20$ and replaces the initial extended fault at high Z side at 460 kyr (Figure 24.d). The vertical tensile failure zone at $Z= 1 \sim 3$ (Figure 24.d 3rd row) begin to evolve and assists in the initiation of a new near ridge axis high angle normal fault which connect with the fault at the high Z side (Figure 24.e) at 590 kyr. At 660 kyr (Figure 24.f 3rd row), there is a hint of high angle normal faulting at $Z= 1 \sim 3$ of conjugate plate. But it doesn't develop. At 730 kyr (Figure 24.g 5th row), a dextral (blue) shear zone at the low Z side help

to create the faulting pattern seen at 780 kyr (Figure 24.h 3rd row), a concave termination with a wavelength of 10 kilometers and it has the potential to create a large wavelength corrugation. Meanwhile, at the low Z side, near the ridge axis, there is an antithetic fault forming at the hanging wall of the detachment and it later propagates to high Z side (Figure 24.i). From 820 kyr to 880 kyr, the antithetic fault evolves to near ridge axis normal fault and connects with the detachment at the high Z side (Figure 24.j). In addition, a tensile failure shows its hint at the low Z side ($Z = 1 \sim 5$) of the conjugate plate.

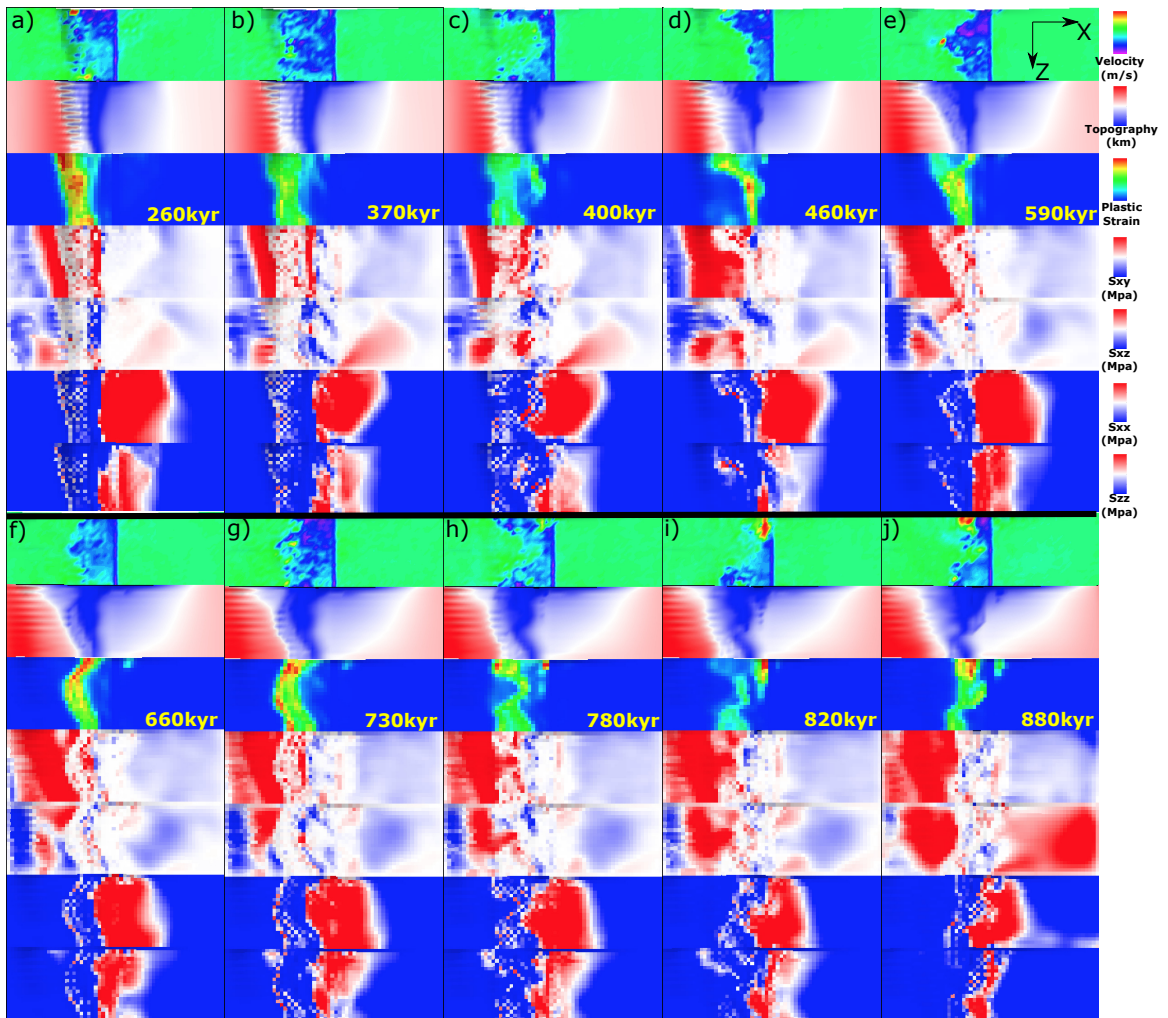


Figure 24: M58SqrtT1 (Table 2) faulting and stress evolution with respect to time.

M58SqrtT2 As shown in Figure 25, at 195 kyr (Figure 25.a), due to transtensional stress at low Z side ($Z = 1 \sim 6$), several corrugations begin to evolve. At conjugate

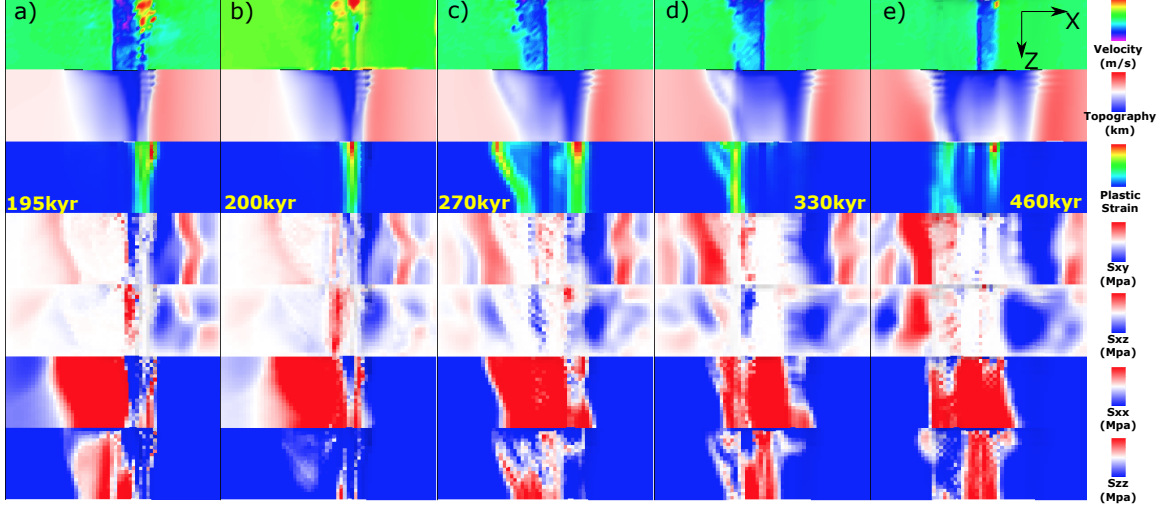


Figure 25: M58SqrtT2 (Table 2) faulting and stress evolution with respect to time.

plate, dipping toward axis shear zone σ_{xy} (red at 4th row) show its curve and keeps accumulating. σ_{xx} is also accumulating on the conjugate plate. Between 195 kyr (Figure 25.a) and 200 kyr (Figure 25.b), there is a cut back. At 270 kyr (Figure 25.c), immediately above and following the curved shape shear σ_{xy} zone on the left hand side of the ridge axis, a new fault begin to evolve and replace the initial fault on the right. At 330 kyr (Figure 25.d), at the low Z side, a new near axis high angle normal fault take the place of initial further away from ridge axis fault partly due to rotational force from along ridge coupling. At 460 kyr (Figure 25.e), another normal fault begin to evolve on the right hand side of the ridge axis.

3.5 Effects of the range of M variation

So far, we have three ranges for M variations along the ridge axis (M28, M57 and M58) with same segment length of 20km. Among the 12 available models, two M58 models and the constant $M= 0.8$ model with type 2 weakening produce fault alternation while others do not. Generally, M57 and M58 models create a median valley much narrower and shallower than that of M28 models. $\frac{dM}{dz}$ is larger for M28 than M58 and M57.

3.5.1 M28SinT1 versus M57SinT1 versus M58SinT1

M57SinT1 versus M58SinT1 For description of M57SinT1 evolution with respect to time, please refer to Section 3 and Figure 20. For description of M58SinT1 evolution with respect to time, please refer to Section 3.4.1 and Figure 22. Comparing M57SinT1 and M58SinT1, the major difference is that the faulting pattern evolution for M58SinT1 is much more dynamic with a higher frequency of secondary faults, cut back and offsetted fault segments connection. For M58SinT1, the new secondary near ridge axis normal or antithetic faults usually replace the existed one. However, for M57SinT1, diking is not strong enough to create big enough stress perturbation along the ridge axis for secondary or antithetic faults to take the place of the original one. At the low Z side, near ridge axis antithetic fault only helps to accommodate tensional stress which help maintain a high angle normal fault with near to ridge axis termination while the termination at the high Z side gradually move off axis. This creates a OCC with larger dome at lower magma supply side than that of higher magma supply side which is opposite to the shape of OCC created by M58SinT1.

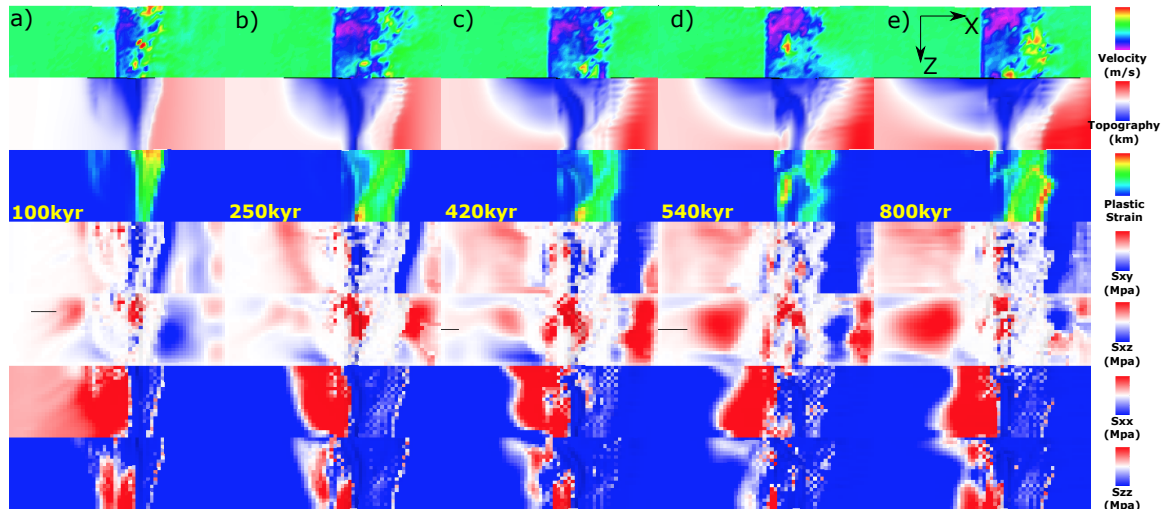


Figure 26: M28SinT1 (Table 2) faulting and stress evolution with respect to time.

M28SinT1 As shown in Figure 26, faulting evolution is much less dynamic than that of M58SinT1. Faulting keeps on the right hand side of the ridge axis. Only one secondary fault is formed at around 540 kyr (Figure 26.d). Initially, at 100 kyr (Figure 26.a), at the low Z side, the normal shear zone at conjugate plate takes up part of the extension and leave a dent in the topography. But it doesn't last long. The initial breakaway of the detachment extends further away from ridge axis with four elements in along ridge axis offset at 250 kyr (Figure 26.b). At 420 kyr, at the high Z side, a hint of new near ridge axis high angle normal fault begin to show up. It develop into a secondary fault at 540 kyr (Figure 26.d) and propagates toward high Z side. This results in a sinistral shear zone (red region in 5th row). At the low Z side ($Z = 1 \sim 3$), a tensile failure can be seen and it take up part of the extension at the low Z side which results in the recede of termination at the low Z side as seen at 800 kyr (Figure 26.e) while the termination at higher Z side extends further away from the ridge axis.

3.5.2 M57SinT2 versus M58SinT2

For description of M57SinT2 evolution with respect to time, please refer to Section 3 and Figure 21. For description of M58SinT1 evolution with respect to time, please refer to Section 3.4.1 and Figure 23. A major difference is that M57SinT2 does not create alternating normal faults on each side of the ridge axis while M58SinT2 does. *XT: Why this seemingly small change could lead to such a to the first order difference in model behaviors?*

3.5.3 M28LinT1 versus M57LinT1

For description of M28LinT1 evolution with respect to time, please refer to Section 3.1.

M57LinT1 As shown in Figure 27, between 160 kyr (Figure 27.a) and 162.5 kyr (Figure 27.b), there is a cut back. The corrugation is very severe and have a discrete distri-

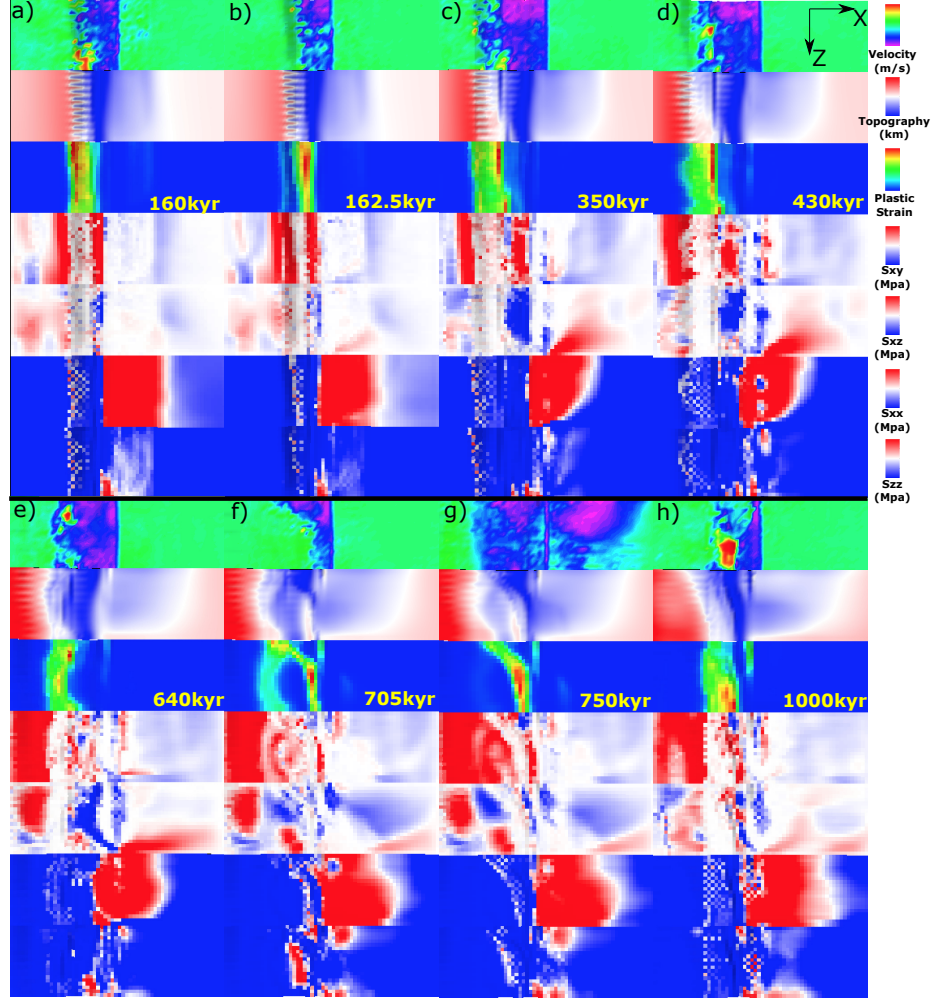


Figure 27: M57LinT1 (Table 2) faulting and stress evolution with respect to time.

bution with one element width as its wavelength. The frontier of breakaway also shows discrete distribution of σ_{xx} and σ_{zz} alternating between tension and compression which might be the reason for the undulating topography. At 350 kyr (Figure 27.c 3rd row), the two offsetted red line indicates tensile failure at the termination and the shorter one at the high Z side helps maintain a near ridge axis high angle normal fault. At 430 kyr (Figure 27.d), the presence of vertical tensile failure near the ridge axis at the low Z side is responsible for the recede of the front of the plastic strain at $Z = 1 \sim 3$. While at $Z=5 \sim 10$, the breakaway keeps extending further away from the ridge axis. This curved front results in a curved topography as seen in 640 kyr (Figure 27.e) and is also responsible for the large dextral shear (blue) zone (5th row). At 705 kyr (Figure 27.f), a new near ridge axis

secondary fault begin to evolve and replace the original one at high Z side with a length of \sim 15 kilometers. The secondary fault also connect with the further away from ridge axis original fault at low Z side. The topography at 1000 kyr (Figure 27.h) is a result of the curved and later connected fault. The frontier of the plastic strain at high Z side soon catch up with that at the low Z side due to the presence of a tensile failure zone at the low Z side that has taken up part of the extension.

3.5.4 M28SqrtT1 versus M58SqrtT1

For description of M28SqrtT1 evolution with respect to time, please refer to Paragraph 4 and Figure 32.

For description of M58SqrtT1 evolution with respect to time, please refer to Paragraph 3.4.2 and Figure 24.

3.5.5 M57SqrtT2 versus M58SqrtT2

For description of M58SqrtT2 evolution with respect to time, please refer to Paragraph 3.4.2 and Figure 25.

The major difference between M57SqrtT2 and M58SqrtT2 is that M57SqrtT2 keeps faulting at the same side of the ridge axis while M58SqrtT2 alternates.

M57SqrtT2 For M57SqrtT2, there are totally six small scale cut back happen at 282.5 kyr, 290 kyr, 365 kyr, 452.5 kyr, 482.5 kyr and 540 kyr respectively (the model stops at 540 kyr). As shown in Figure 28, the fault keeps on the left hand side of the ridge axis. At 200 kyr (Figure 28.b), a new near ridge axis high angle normal fault begin to evolve and take the place of the initial one. As the fault evolve, a transient stage of discontinuous abyssal hill is produced at the low Z side as seen at 225 kyr (Figure 28.c). The fault propagate toward high Z side and cut through the plate at \sim 245 kyr (Figure 28.d) when sawtooth shape topography at the low Z side (2nd row) is created by sawtooth shape σ_{xx}

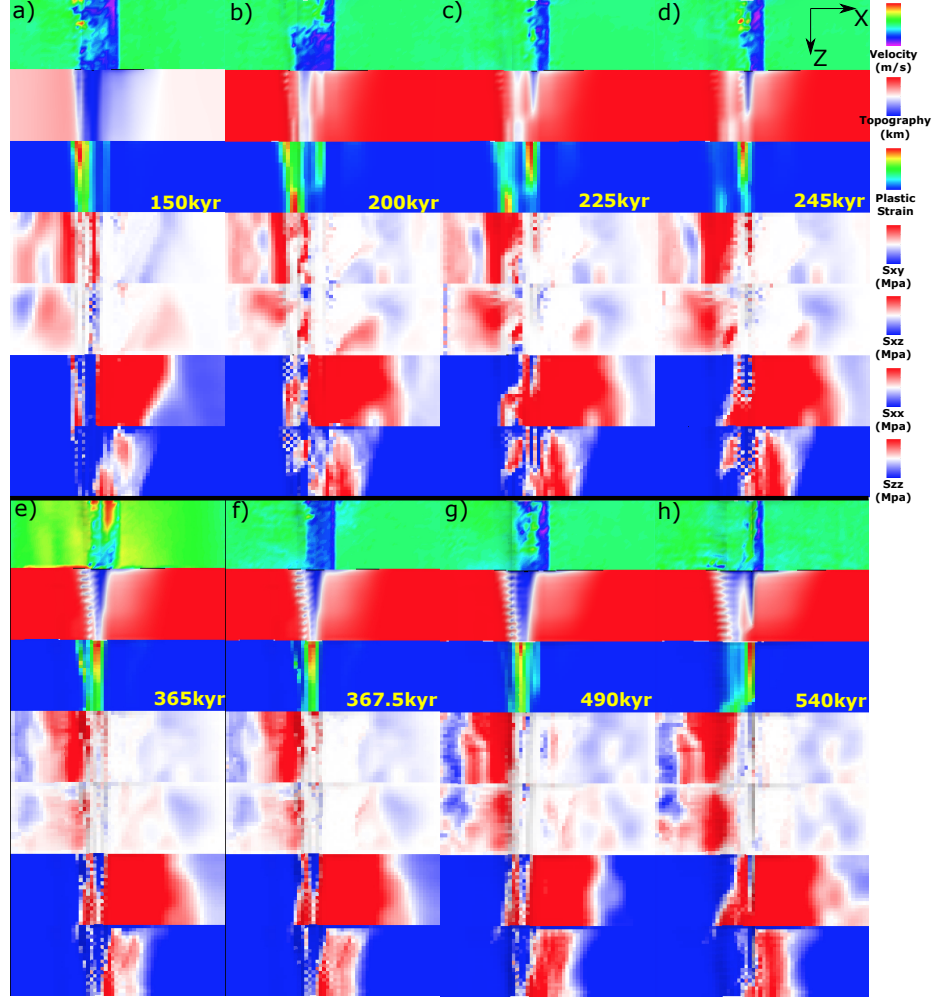


Figure 28: M57SqrtT2 (Table 2) faulting and stress evolution with respect to time.

(6th row) and σ_{zz} (7th row). Between 365 kyr (Figure 28.e) and 367.5 kyr (Figure 28.f), there is a cut back. At 490 kyr (Figure 28.g), there is new near ridge axis antithetic fault on the hanging wall which terminates the old fault and develops into a vertical near ridge axis tensile failure as seen at 540 kyr (Figure 28.h).

3.6 Summary of Results

There are several behaviors that are controlled by the model parameters. Generally, only M58 models with type 2 weakening produce alternating faults on both side of the ridge axis. All the models show corrugations. As for faulting patterns in terms of evolution fre-

quency, usually Square root is more dynamic than Sinusoidal than Linear, M58 is more dynamic than M57 than M28.

Following tables are a summary of the model behaviors with respect to different setup parameters.

Table 3: Model behaviors in short.

A	Alternating Fault	C	Corrugation	SL	Shear Topography Low
NA	Not Alternating	SF	Secondary Fault on one side	CB	Cut Back
DD	Double Dome	AM	Atlantis Massif Shape		

Based on the 11 models with M variation, we observed eight first-order behaviors as shown in Table 3.

Table 4: Linear functional form.

M range Type \ Type	M28	M57	M58
Type one	NA; C; SL; SF _{1500kyr} ; DD	NA; C; SF _{1380kyr} ; CB _{330kyr} ; AM(opposite z)	
Type two			

Table 5: Sinusoidal functional form.

M range Type \ Type	M28	M57	M58
Type one	NA; C; SL; SF _{995kyr}	NA; C; SL; SF _{760kyr;1320kyr} ; CB _{520kyr} ; AM	NA; C; SL; CB _{510kyr} ; SF _{760kyr;1140kyr;1990kyr}
Type two		NA; C; SL; SF _{680kyr} ; CB _{905kyr}	A _{450kyr;600kyr} ; C(only at low M); CB _{990kyr}

Table 6: Square root functional form.

M range Type \	M28	M57	M58
Type one	NA; C; SL; $CB_{205kyr;330kyr;1025kyr}$		NA; $C_{1770kyr}$ (due to shear with dif wave length); SF_{860kyr} (high M); $SF_{1190kyr}$ (low M)(Dog Bone); $SF_{1690kyr}$
Type two		NA; C; $SF_{435kyr;1060kyr};$ $CB_{585kyr}; CB_{735kyr};$ $CB_{910kyr}; CB_{970kyr}$	$A_{550kyr;920kyr}; C;$ CB_{400kyr}

4 Discussion

Generally, all models forms a median valley that deepens and widens toward the lower M side (Figure 8) except the reference model with constant $M = 0.8$ (Figure 13). The topography observed in our models, to the first order, is controlled by the spatial and temporal distributions of faulting and to the second order, results from elastically deformation (e.g. The gradual deepening and widening of the median valley; The bending of the crust at the footwall side of the detachment fault results in a domal shape of the fault interface as a mechanism for producing the dome shape of OCCs).

The pattern of the deformation (faulting and elastic deformation) is controlled by the evolving stress in the crust in terms of its distribution and magnitude. The stress evolution is a result of the interaction processes between tectonics and magmatism. Due to constant seafloor spreading, tensional stress orthogonal to the ridge-axis in the crust keeps accumulating. At the same time, along ridge-axis varying diking partially accommodates the stress from far field extension and perturbs the homogeneity state of stress distribution along the ridge-axis. Accumulated stress will be largely released when the tensile or shear failures establish.

Since the model behavior is very complicated. We will focus on the effects being brought by the along ridge-axis variation in diking. Thus, it is worth considering a thought experiment with two end members: One, the along ridge-axis coupling is rigid, so that even along ridge axis variation in M exist, once a fault determined to develop, it will cut through the whole model domain along the ridge-axis(Z-axis) simultaneously. The other end member is that there is totally no coupling along the ridge-axis. So that each slice of crossection profile across the ridge behave separately without being influenced by its neighbour to a extreme that the model behavior is just a combination of 20 pseudo-2D models piled up along ridge-axis with their own M . (IMPORTANT: this suggests the importance and urgency for making clear conclusion and results description for previous pseudo-2D models results. However, one difficulty here is that the characteristic fault off-

set ΔX_c is different between 2D and 3D models.)

4.1 Discussion on Reference models

4.2 Cut Back

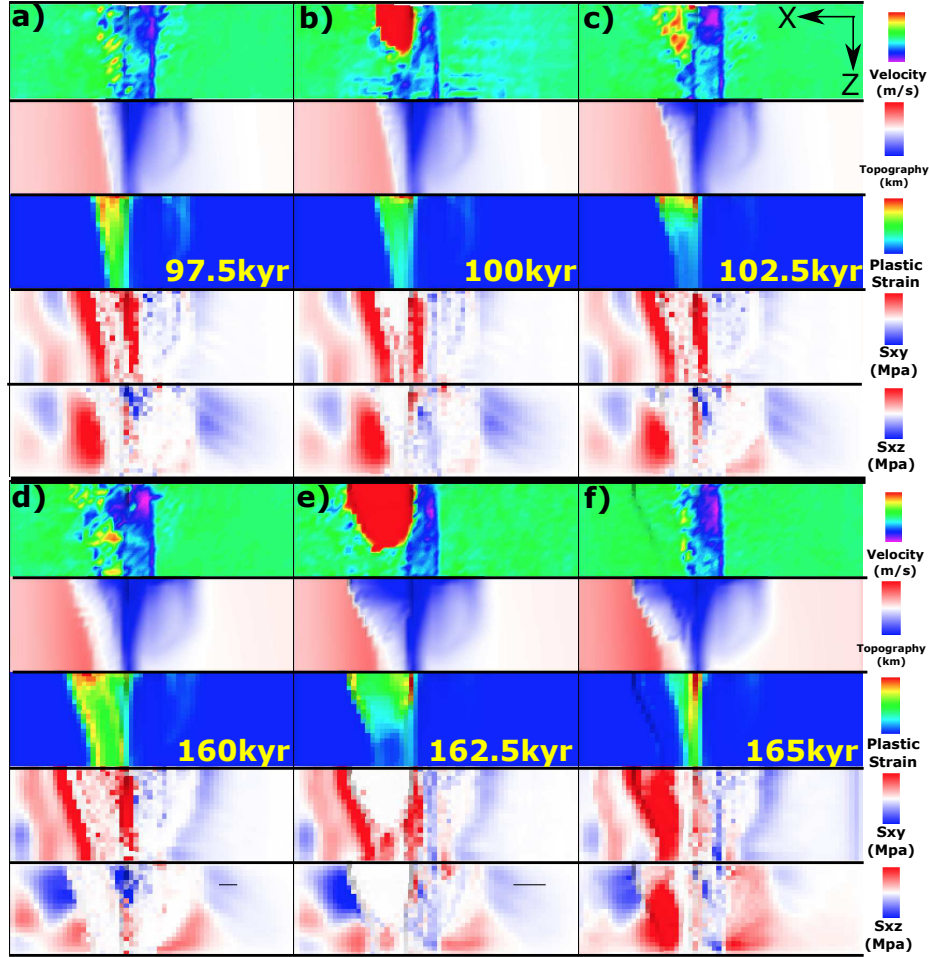


Figure 29: M28SqrtT1 (Table 2). Cut back behaviors in square root functional form model with different time.

The cut back happens mostly in the square root model. Since the linear model and the square root model have more obvious difference in terms of the cut back behavior, here, we only compare linear and square root. There are several factors contribute to the cut back behavior. First, at the higher M side, the amount of diking for the square root model is ubiquitously larger than that of the linear one (Figure 15). This leads to a slower bend-

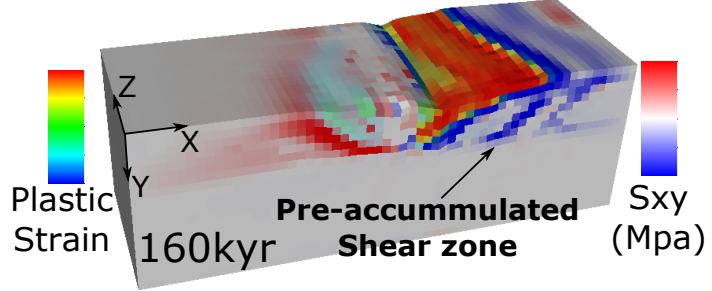


Figure 30: M28SqrtT1 (Table 2). Square root functional form model at 160kyr. Pre-accumulated shear zone increase the shear force and cut the weak detachment front tip

ing detachment at the high M side for the square root model. Second, the total length of the ridge segment with $M > 0.5$ for the square root model is also longer than that of the linear one (Figure 15). This results in that at the low M side, σ_{xz} is focused at low Z adjacent to the ridge-axis (Figure 17.e), however for linear is spread out to Z higher than 10. Third, due to higher value of $\frac{dM}{dZ}$ for square root when $Z < 5$, the along ridge-axis shear σ_{xz} for square root will be accumulating faster, which produces larger strike-slip force to cut the hanging wall at the low M side. Fourth, as observed in the model (Figure 17.c), the parallel to spreading direction offset between breakaways along the ridge-axis is 4km for the square root model compared to 3km for the linear model. This causes the square root model to experience bigger shear stress σ_{xy} both immediately beneath and above the fault interface at the low M side (Figure 17.d). Fifth, as shown in Figure 10, due to bending of the crust at the footwall side, below the blue neutral plane, $\sigma_{xx} > 0$, meaning tensile stress being accumulated as fault develops. The resulting force tends to unbend the bent crust and drag down the connecting surface (the future decoupled hanging wall). All five factors together assist in the decouple of the hanging wall at the low M side as described in detail in the next paragraph.

In the Figure 29, the hanging wall rebounds backwards to the dike in a high velocity (Figure 29.b,e (velocity)) accompanied with a sudden topography drop (Figure 29.b) compared to c); d) compared to e) (in the second row)). This behavior is triggered when

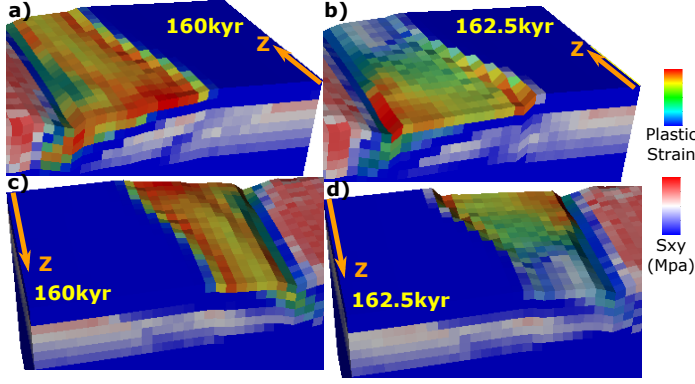


Figure 31: M28SqrtT1 (Table 2). Bending stress drop in the crust close to dike due to cut back behavior.

the front tip of the weak detachment extends further away from the ridge-axis and reaches a pre-accumulated shear zone (Figure 30). The pre-accumulated shear zone adds extra shear force to the weak (Figure 29.d(third row: plastic strain)) as well as shear stresses accumulated (Figure 29.d(fourth and fifth row: σ_{xy} and σ_{xz})) fault interface and together with the five factors mentioned in the previous paragraph result in the cut back behavior. The cut back produces a continuous high angle fault scarp with a relief of $\sim 1\text{ km}$ aligns to the initial breakaway and extends for about 20 kilometer in length (Figure 29.e (second row: topography)). Its distance to the ridge-axis varies along the Z-axis and this result can be used to indicate the magma supply variation in the nature. ^{XT:}To be discussed in observation comparison section. as a reminder

During the cut back process, the tensional bending stress are released at the low M side ($0 < Z < 7$) in the left tip of the bended crust (Figure 31.a compared to b), however, in the higher M side, the tensional bending stress keeps accumulating due to the far field extension (Figure 31.c compared to d). This behavior assists in the decouple between low M and high M side hanging walls.

Once the cut back happens at 162.5kyr, the σ_{xy} , σ_{xz} and σ_{xx} are released (Figure 29.e (fourth and fifth row: σ_{xy} and σ_{xz})). The plastic strain near the ridge-axis at low M side reaches a maximum of ~ 0.9 (Figure 29.e (third row: plastic strain)) compared to ~ 0.3 before and after. This is due to the sudden backward motion squeezes the end element of

the hanging wall near the ridge-axis and later be released by the continuous extension.

After the cut back, the termination of the detachment recedes backwards for about 7 kilometer towards the ridge-axis (Figure 29.f (third row: plastic strain)) (termination fronts are always consistent with tension stresses in σ_{xx} and σ_{zz} as well as with plastic strain front(due to healing, high plastic strain region corresponds only to region with continuously deformation) (Figure 17 and Figure 18)). This behavior helps maintain a high angle normal fault. Different from the linear and sinusoidal models that the detachments at the low M side will rotate to a very low angle, square root model doesn't. In addition, σ_{xy} and σ_{xz} soon fill in the area between cut back created fault scarp and the new termination (Figure 29.f (fourth and fifth row: σ_{xy} and σ_{xz}) because σ_{xy} always accumulates immediately beneath the normal fault interface and the red σ_{xz} left to the new termination is due to the along ridge-axis variatioin in the rate of fault slip (low M side larger).

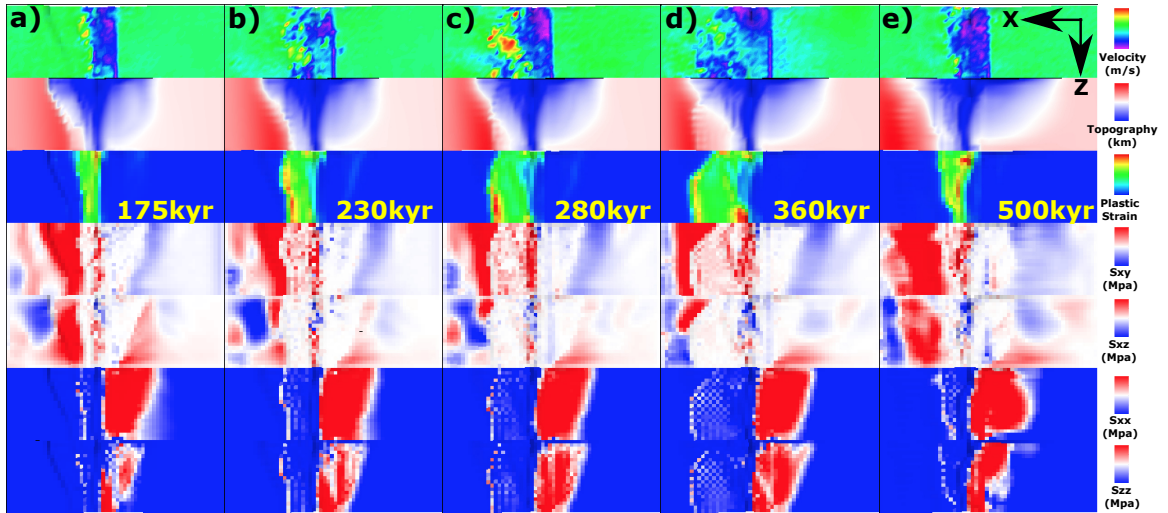


Figure 32: M28SqrtT1 (Table 2). New fault front chase after initial abandoned breakaway.

There is one phenomenon very interesting and counter-intuitive that worth describing here. After the cut back, and termination retreat, the evolution of the detachment fronts is opposite to initiall or to the general behavior in the linear and sinusoidal models. The termination front at the high M side extends faster and further after the cut back (Figure 32). This is partly related to the unbending decouple phenomenon we described ealier that the

tensional stress are released at the low M side but continues to accumulate in the high M side during the cut back unbending in the low M side. Since the tensional stress is released in the low M side, it needs time to accumulate to where it was and then start from there to drag the new near ridge-axis fault away from the ridge-axis while at the high M side the increasing tensional stress will directly lead to a fast extending fault front. Thus create the behavior. *^{XT}: One question is, how to explain that the fault front is moving much faster than the initial abandoned breakaway? New fault front soon reach the old breakaway.*

This phenomenon is largely responsible for the corrugations observed. It creates a “X” shape “scan” that first “scan” the topography with faster low M side (Figure 29.d and e) and then with faster high M side (Figure 32.c and d). This results in curved terminations with hundreds to several kilometers wavelengths that directly create parallel to spreading direction corrugations.

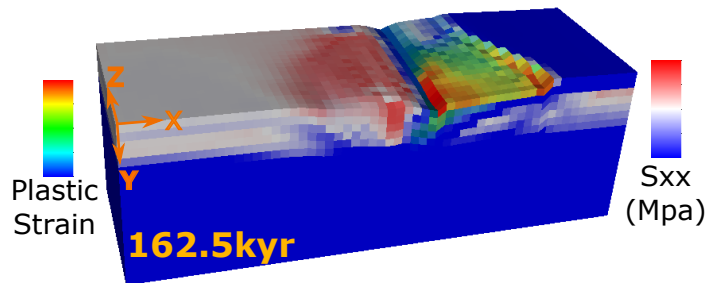


Figure 33: M28SqrtT1 (Table 2). Higher σ_{xx} in the median valley of conjugate plate at low M side.

In addition, the higher σ_{xx} in the median valley of conjugate plate at low M side (Figure 33) is due to the brittle crust is thinnest at the median valley, thus when same amount of force propagates from far field extension to the center median valley, the stress will increases.

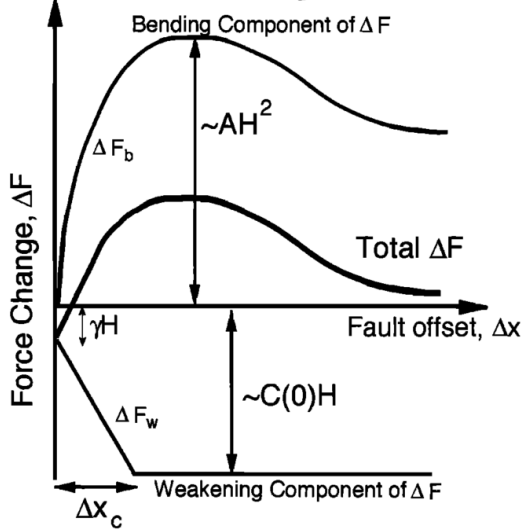


Figure 34: Trade-off between change in bending force ΔF_b and weakening in the fault interface ΔF_w . H is the thickness of the brittle crust and γ is the size of initial weak perturbation and A defines the maximum bending force change. (For more details, please refer to [Lavier et al., 2000])

4.3 Fault Alteration

4.3.1 Trade-off between bending and weakening

Before we move on to each of the pairs, the framework studied by [Lavier et al., 2000] needs to be mentioned here for better understanding the model behaviors observed in our model results. There is a trade-off between change in bending force ΔF_b as a function of fault offset ΔX and force change ΔF_w as a function of ΔX due to strain weakening. As described in [Lavier et al., 2000], higher characteristic fault offset (ΔX_c) or slower strain weakening results in multiple faults rather than only one fault lasting. Whether conjugate fault and even multiple faults can be produced depends on the local stress condition. The strength weakening of the existed fault combines with how much bending force resists the fault to keep offsetting play a major role in determining the stress state at the other areas. As the sea-floor keeps spreading and ΔX increasing, the change in bending force ΔF_b increases and the strength at the fault interface decreases due to weakening ΔF_w (Figure 34). If the net force change $\Delta F = \Delta F_b + \Delta F_w$ is positive, it means that it is

getting harder and harder to maintain the existing fault and stress will begin to accumulate at the other areas which eventually break another fault. ΔF_b initially increases fast with respect to ΔX and then when the breakaway bends over, it reaches its peak value and begins to decrease a little and maintains at a constant value. If the strain weakening is fast enough that the net effect force ΔF is always negative, then most of the stress will be released by the existing fault and thus no conjugate or multiple faults will be created.

Our model results verify this analysis that only Type two weakening (slower weakening with higher ΔX_c) can produce an alternating normal fault on the conjugate plate.

Based on the previous experience in pseudo-2D models and [Lavier et al., 2000], when $M > 0.5$, the frequency of normal faulting alternation is higher for higher characteristic fault offset (ΔX_c) of Type two weakening compared to Type one weakening. However, for the reference model two, M88ConT2 (Table 2), interesting enough, when comparing pseudo-2D and 3D models with Type two weakening under case of $M = 0.8$, even though the 3D Model has a larger ΔX_c of 1km than that of pseudo-2D model of 0.5km, the 3D model M88ConT2 has a lower frequency of faulting alternation. Since M is constant 0.8 along the ridge-axis, the effect of along ridge coupling that resists alternation need not be considered. One possibility is that the resisting bending force increase in a higher rate than linear with respect to increasing the length of the ridge segment (Z_{max} km).

4.3.2 Alternating on conjugate plate

The fault alternation behavior observed in pseudo-2D models in cases $M > 0.5$ is much more complicated in 3D models. The results show that only Type two weakening with M58 will result in an alternating faulting pattern. XT : integrate the area of $M > 0.5$ with respect to Z to see if there is any quantitative analysis available.

4.3.3 Secondary near-axis normal fault

The secondary near axis high angle normal fault is another common observation of the models. As shown in Figure 8, at the ridge axis with $M > 0.5$ (i.e. $Z > 10$), the existing normal fault will be pushed away from the ridge-axis due to excessive diking, as its mechanism has been mentioned in the introduction chapter, another new near axis normal fault is created at around 650kyr. As it evolves, the initial detachment fault becomes inactive (the transparent view of plastic strain shown in the right corner inset of time 880kyr). This secondary fault creates another dome and its composition is more likely to be volcanic rather than ultramafic, however, as it evolves, if it can last long, lower crust and upper mantle material can be exhumed to the surface. The composition of the domes observed at Kane magamullions is similar to this mechanism that ultramafic Babel dome is on the West and crustal inside-corner high on the East.

4.3.4 Effect of along ridge-axis coupling

The along ridge-axis coupling allowed the normal fault at the high M side ($M > 0.5$) to last for a long time and become a detachment that can produce an OCC. This behavior is different from previous 2D studies that only $M=0.3 \sim 0.5$ can make OCCs and it also provides an alternative explanation for reconciling the gap between 2D model and observation described in [Olive et al., 2010]. Instead of magma injecting below brittle ductile transition, even injecting in the crust, due to along ridge coupling, model can still create OCC for high magma supply. Find the observation evidence for high M OCC from refs of Olive2010. As mentioned in the abstract of Olive2010, ref4-11 show a spectrum of magma supply.

4.4 Corrugations

There are two contributing factors, for one, trans-extenstional stresses are created due to offset of the breakaway as well as the variation in fault displacements along the ridge axis; for the other, the variation of the positions of the terminations of the detachment faults along the ridge-axis creates anastomosing faults that is mentioned in [Smith et al., 2014]. This anastomosing faulting behavior is largely responsible for corrugations in our models.

The stress at the tips of the breakaways is generally tensional in both parallel and orthogonal directions to the ridge-axis. (Figure 17.f,g)

4.4.1 Wavelength of corrugations

4.5 Influence of healing

4.6 Comparing model results with nature observation

4.6.1 Cut back at 13°N Mid-Atlantic Ridge (M28SqrtT1)

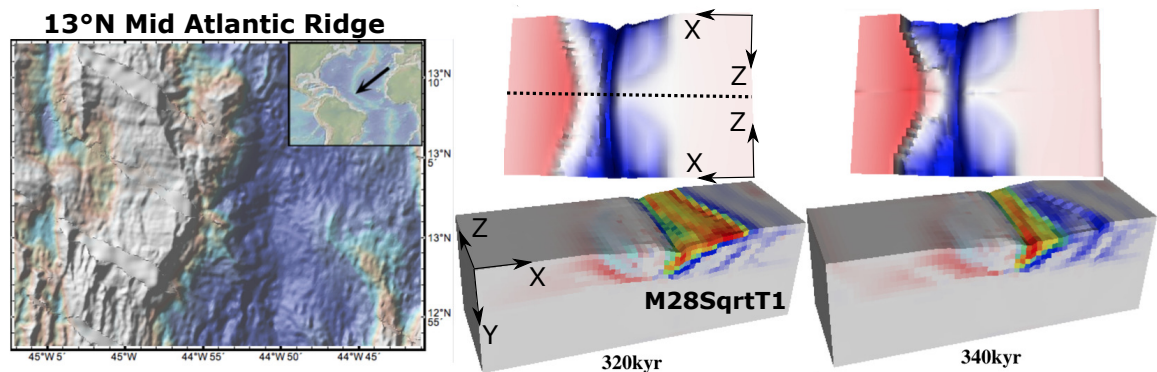


Figure 35: Comparing nature observation at 13°N Mid-Atlantic Ridge to the Cut back behavior of model M28SqrtT1. The model topography is a mirror symetric flip according to the dash line, it reveals the case of M varies in a square root functional form from 0.2 to 0.8 to 0.2. For discussion on cut back formation mechanism, please refer to Section 4.2. The bathymetry is from GeoMapApp [Ryan et al., 2009].

The cut back behavior in M28SqrtT1 model creates a fault scarp of $\sim 1\text{km}$ in relief,

40km in length along the Z axis. Note that the fault scarp corresponds to initial formed breakaway. The topography at 13°N Mid-Atlantic Ridge also has a fault scarp with very similar geometry with ~1km in relief. Due to the variation in diking along the ridge-axis, a sandglass shape of median valley is also produced in the model where the narrowest center corresponds to the region with high magma supply ($M=0.8$). This sandglass shape is also frequently observed in the nature along the Mid-Atlantic Ridges.

4.6.2 Double dome at 23°N Mid-Atlantic Ridge (Kane Megamullions) (Several models)

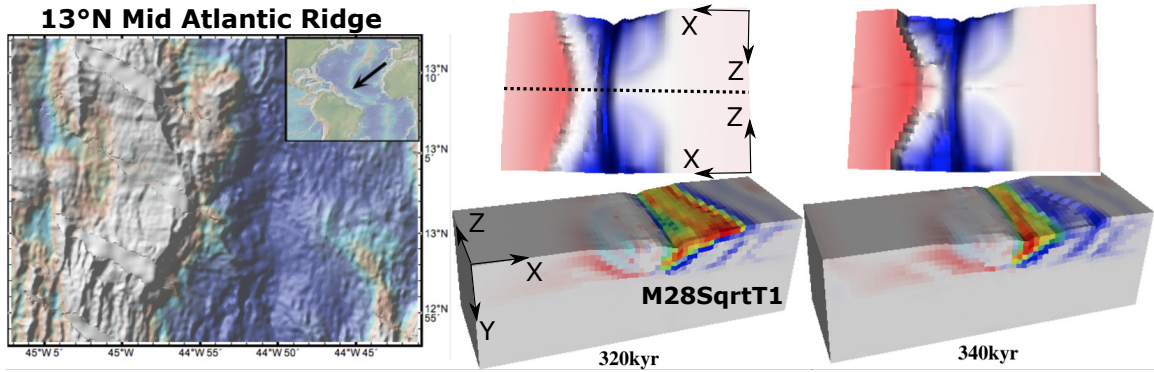


Figure 36: Comparing nature observation at 13°N Mid-Atlantic Ridge to the Cut back behavior of model M28SqrtT1. The model topography is a mirror symmetric flip according to the dash line, it reveals the case of M varies in a square root functional form from 0.2 to 0.8 to 0.2. For discussion on cut back formation mechanism, please refer to Section 4.2.

4.6.3 Atlantis Massif Shape at 30°N Mid-Atlantic Ridge ()

4.6.4 Shear low

4.6.5 Corrugations

4.7 Model Limitation

4.7.1 Fixed thermal structure effects and justification

Thermal conduction rate for $\kappa = 6\text{mm}^2/\text{s}$ material is $1.8\text{e}5 \text{ km/Myr}$, four magnitude faster compared to spreading rate of 2.5km/Myr .

4.8 Recommendation for Future Research

5 Conclusions

Bibliography

- G. Baines, M. J. Cheadle, B. E. John, and J. J. Schwartz. The rate of oceanic detachment faulting at atlantis bank, sw indian ridge. *Earth and Planetary Science Letters*, 273(1-2):105–114, Aug. 2008. ISSN 0012821X. doi: 10.1016/j.epsl.2008.06.013.
- R. Buck, L. Lavier, and A. Poliakov. Modes of faulting at mid-ocean ridges. *Nature*, 434(7034):719–23, 2005. ISSN 1476-4687. doi: 10.1038/nature03358.
- S. M. Carbotte, D. K. Smith, M. Cannat, and E. M. Klein. Tectonic and magmatic segmentation of the global ocean ridge system : a synthesis of observations. *Geological Society of London*, 2015.
- Y. J. Chen and J. Lin. Mechanisms for the formation of ridge-axis topography at slow-spreading ridges: A lithospheric-plate flexural model. *Geophysical Journal International*, 136:8–18, 1999. ISSN 0956540X. doi: 10.1046/j.1365-246X.1999.00716.x.
- E. Choi, L. Lavier, and M. Gurnis. Thermomechanics of mid-ocean ridge segmentation. *Physics of the Earth and Planetary Interiors*, 171(1-4):374–386, Dec. 2008. ISSN 00319201. doi: 10.1016/j.pepi.2008.08.010.
- C. M. R. Fowler. *The solid earth: an introduction to global geophysics*. Cambridge University Press, 2004.
- S. Kirby and A. K. Kronenberg. Rheology of the lithosphere: Selected topics. *Reviews of Geophysics*, 25(6):1219–1244, 1987.
- L. L. Lavier, W. R. Buck, and A. N. B. Poliakov. Factors controlling normal fault offset in an ideal brittle layer. *Journal of Geophysical Research*, 105(B10):23431, 2000. doi: 10.1029/2000JB900108.
- J. Lin, G. M. Purdy, H. Schouten, J.-C. Sempere, and C. Zervas. Evidence from gravity

data for focused magmatic accretion along the Mid-Atlantic Ridge. *Nature*, 344:627–632, 1990. ISSN 0028-0836. doi: 10.1038/344627a0.

J.-A. Olive, M. D. Behn, and B. E. Tucholke. The structure of oceanic core complexes controlled by the depth distribution of magma emplacement. *Nature Geoscience*, 3(7):491–495, June 2010. ISSN 1752-0894. doi: 10.1038/ngeo888.

W. B. F. Ryan, S. M. Carbotte, J. O. Coplan, S. O’Hara, A. Melkonian, R. Arko, R. A. Weissel, V. Ferrini, A. Goodwillie, F. Nitsche, J. Bonczkowski, and R. Zemsky. Global multi-resolution topography synthesis. *Geochemistry, Geophysics, Geosystems*, 10, 2009. ISSN 15252027. doi: 10.1029/2008GC002332.

D. K. Smith, H. Schouten, H. J. B. Dick, J. R. Cann, V. Salters, H. R. Marschall, F. Ji, D. Yoerger, A. Sanfilippo, R. Parnell-turner, C. Palmiotto, A. Zhelezov, H. Bai, W. Junkin, B. Urann, S. Dick, M. Sulanowska, P. Lemmond, and S. Curry. Development and evolution of detachment faulting along 50 km of the mid-atlantic ridge near 16.5°n. *Geochemistry Geophysics Geosystems*, pages 4692–4711, 2014. doi: 10.1002/2014GC005563. Received.

M. Tolstoy, A. J. Harding, and J. A. Orcutt. Crustal Thickness on the Mid-Atlantic Ridge: Bull’s-Eye Gravity Anomalies and Focused Accretion. *Science*, 262(October):726–729, 1993. ISSN 0036-8075. doi: 10.1126/science.262.5134.726.

B. E. Tucholke, M. D. Behn, W. R. Buck, and J. Lin. Role of melt supply in oceanic detachment faulting and formation of megamullions. *Geology*, 36(6):455, 2008. ISSN 0091-7613. doi: 10.1130/G24639A.1.

D. L. Turcotte and G. Schubert. *Geodynamics*. Cambridge, 2002.